Article
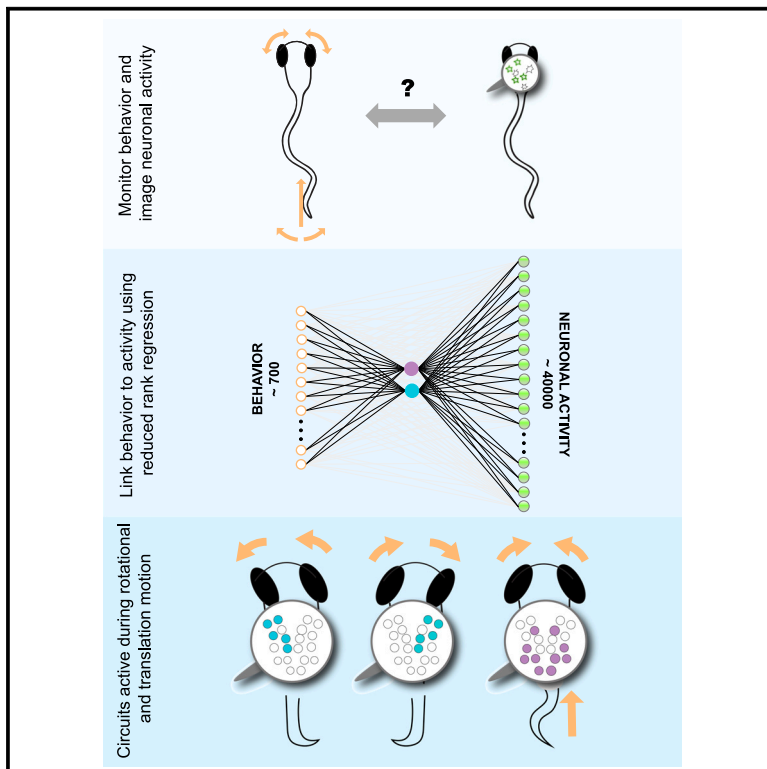
Dimensionality reduction reveals separate translation and rotation populations in the zebrafish hindbrain

Graphical abstract

Authors

Claudia E. Feierstein, Michelle H.M. de Goeij, Aaron D. Ostrovsky, Alexandre Laborde, Ruben Portugues, Michael B. Orger, Christian K. Machens

Correspondence

claudia.feierstein@neuro.fchampalimaud.org (C.E.F.),
michael.orger@neuro.fchampalimaud.org (M.B.O.),
christian.machens@neuro.fchampalimaud.org (C.K.M.)

In brief

Feierstein et al. use visual stimuli that elicit decoupled eye movements and swimming in zebrafish larvae. Combining regression and dimensionality reduction techniques, they show that behavior-related activity in the hindbrain is low dimensional. Neurons form functional and spatial clusters related to vergent and rotational movements.

Highlights

- Bilaterally independent visual stimuli decouple eye movements and elicit swimming

- In the dorsal hindbrain, activity related to the eyes and tail is low dimensional

- Neurons form clusters related to vergent and left/right rotational movements

- Rotation and vergence clusters have distinct anatomical organization

CellPress

Article

Dimensionality reduction reveals separate translation and rotation populations in the zebrafish hindbrain

Claudia E. Feierstein,[1,9,*] Michelle H.M. de Goeij,[1,2,5,8] Aaron D. Ostrovsky,[1] Alexandre Laborde,[1] Ruben Portugues,[3,4] Michael B. Orger,[1,6,7,*] and Christian K. Machens[1,6,7,*]

[1]Champalimaud Neuroscience Programme, Champalimaud Foundation, Lisbon 1400-038, Portugal
[2]Faculty of Medicine, Utrecht University, Utrecht 3584 CG, the Netherlands
[3]Institute of Neuroscience, Technical University, Munich 80802, Germany
[4]Munich Cluster of Systems Neurology (SyNergy), Munich 81377, Germany
[5]Pfizer BV, Capelle aan den Ijssel 2909 LD, the Netherlands
[6]These authors contributed equally
[7]Senior author
[8]Present address: Pfizer BV, Capelle aan den Ijssel 2909 LD, the Netherlands
[9]Lead contact
*Correspondence: claudia.feierstein@neuro.fchampalimaud.org (C.E.F.), michael.orger@neuro.fchampalimaud.org (M.B.O.), christian.machens@neuro.fchampalimaud.org (C.K.M.)
https://doi.org/10.1016/j.cub.2023.08.037

SUMMARY

In many brain areas, neuronal activity is associated with a variety of behavioral and environmental variables. In particular, neuronal responses in the zebrafish hindbrain relate to oculomotor and swimming variables as well as sensory information. However, the precise functional organization of the neurons has been difficult to unravel because neuronal responses are heterogeneous. Here, we used dimensionality reduction methods on neuronal population data to reveal the role of the hindbrain in visually driven oculomotor behavior and swimming. We imaged neuronal activity in zebrafish expressing GCaMP6s in the nucleus of almost all neurons while monitoring the behavioral response to gratings that rotated with different speeds. We then used reduced-rank regression, a method that condenses the sensory and motor variables into a smaller number of "features," to predict the fluorescence traces of all ROIs (regions of interest). Despite the potential complexity of the visuo-motor transformation, our analysis revealed that a large fraction of the population activity can be explained by only two features. Based on the contribution of these features to each ROI's activity, ROIs formed three clusters. One cluster was related to vergent movements and swimming, whereas the other two clusters related to leftward and rightward rotation. Voxels corresponding to these clusters were segregated anatomically, with leftward and rightward rotation clusters located selectively to the left and right hemispheres, respectively. Just as described in many cortical areas, our analysis revealed that single-neuron complexity co-exists with a simpler population-level description, thereby providing insights into the organization of visuo-motor transformations in the hindbrain.

INTRODUCTION

Many organisms exhibit behaviors that compensate for perceived self-motion. Among these behaviors are the optokinetic response[1–4] (OKR), a conjugate movement of the eyes in response to whole-field rotation that helps to stabilize the retinal image, and the optomotor response[5–7] (OMR), a directional movement of the whole body that helps animals to maintain a fixed position. Both OKR[3,8] and OMR[6,7] can be studied in zebrafish from an early age. In response to rotational optic flow, zebrafish execute conjugate movement of the eyes or turning bouts. In response to translational optic flow, zebrafish swim to cancel the optic flow. To engage in either behavior, fish need to disambiguate rotational and translational optic flow and convert them

into appropriate motor commands that compensate for the observed motion.

Horizontal eye movements are controlled by motoneurons residing in the oculomotor and abducens nuclei. Distinct areas in the hindbrain send inputs to these nuclei in the context of OKR and other behaviors. Two main hypotheses have been proposed about the underlying circuitry in vertebrates. Hering's "law of equal innervation" proposes separate circuits for conjugate and vergent eye movements,[9,10] whereas Helmholtz's theory proposes separate circuits for left and right eye movements.[11,12] Evidence for the two hypotheses has remained inconclusive: in the monkey brain, some studies have identified separate areas for conjugate and vergent eye movements,[13,14] while others have pointed to monocular encoding of eye
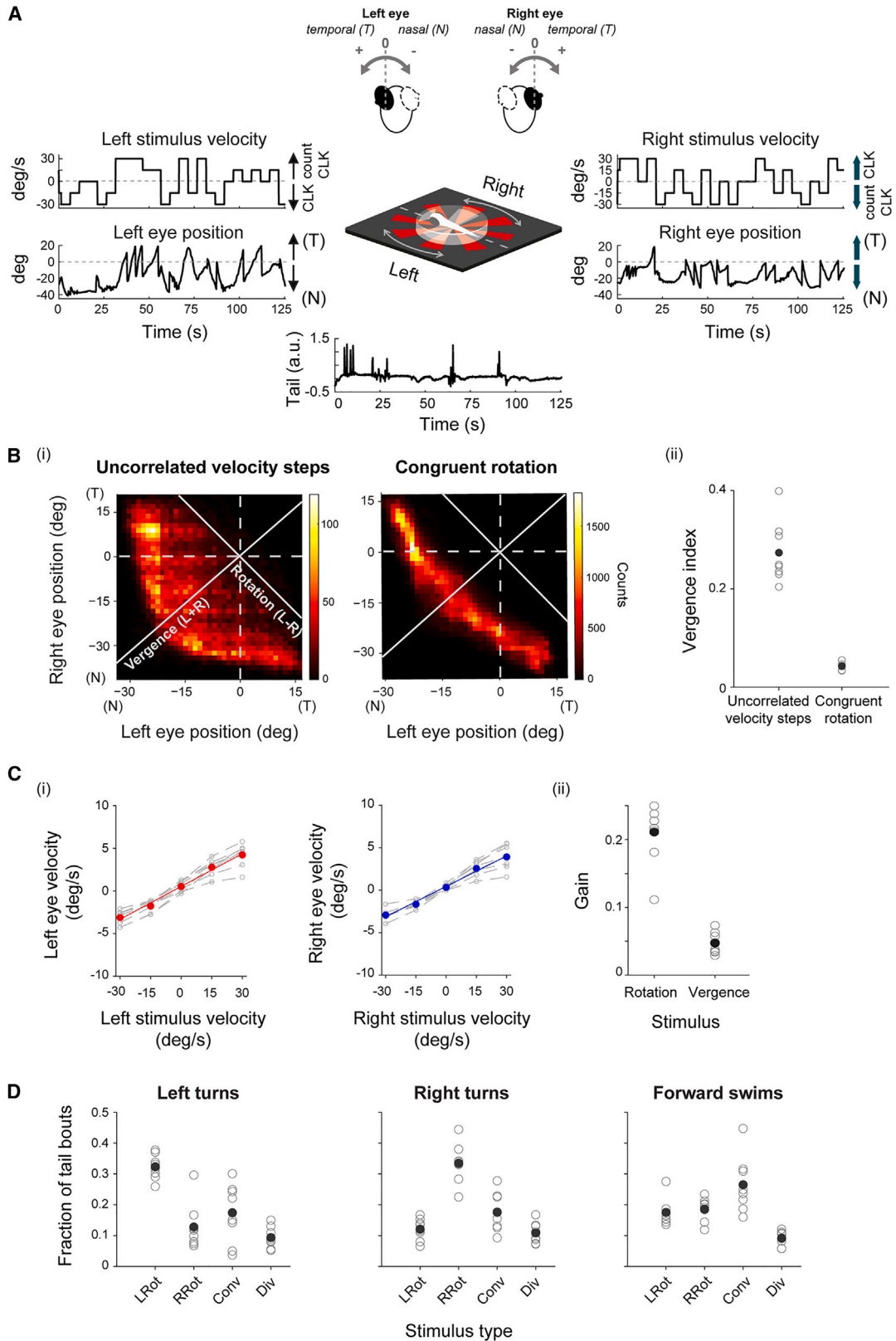
(legend on next page)

movements.[15–17] Similarly, studies in teleost fish find both monocular and binocular encoding of eye position and velocity in all areas of the oculomotor system that have been surveyed.[18–20]

Tail movements are controlled by spinal cord circuits, which receive inputs from reticulospinal neuron groups that mediate forward swimming and turning bouts.[21] The anterior hindbrain, a region that is likely upstream of the reticulospinal system, has also been implicated in the selection of turning direction in different contexts.[22–26] Interestingly, this brain region is also active during spontaneous eye saccades, suggesting that this area could be coordinating eye and tail movement in this behavioral context.[25] Whether other hindbrain areas also mediate both tail and eye movements remains unknown.

While the studies described above have provided important insights into the functioning of these systems, they have largely focused on the analysis of single neurons, showing that neurons in the hindbrain are diversely tuned to monocular or binocular eye position and velocity, or to directional swimming. Heterogeneity of tuning, and specifically the mixing of both sensory and motor parameters, is also a property of many higher-order cortical circuits[27–29] and can often be given a simpler and more intuitive interpretation when studied with methods that reduce the dimensionality of population activity.[30–34] Such methods replace the multitude of single-neuron tuning curves by a few population modes that essentially summarize the activity of a whole population. Zebrafish are an ideal model organism to move beyond single-neuron analysis, because they allow imaging of much or all of the brain at cellular resolution.[25,35–38] Several studies have taken advantage of this, mapping behavioral variables onto large sets of individual neurons and performing functional clustering to identify candidate circuits active in a range of behaviors.[22,23,25,38–41]

Here, we set out to study the hindbrain, an area that has been strongly associated with both eye and tail movements.[18,22–25,38,40,42] The majority of studies of eye-related responses have focused on ventral areas, including the abducens nucleus and the oculomotor integrator. In a previous whole-brain study,[38] however, we identified a population of eye-sensitive neurons located in the dorsal hindbrain, and thus here we further explore this region. We used a set of visual stimuli aimed at dissociating movements of the left and right eyes, thereby eliciting a diversity of behavioral responses that include rotation and vergence eye movements, with accompanying swimming. Using two-photon calcium (Ca)-imaging, we then recorded the activity of tens of thousands of neurons while the fish were behaving. Through a combination of regression and dimensionality reduction, we find that the population activity in the hindbrain related to eye or tail movement is largely restricted to a two-dimensional subspace corresponding to rotation and vergence variables. Based on these dominant activity patterns, we show that neurons in the hindbrain can be separated into three anatomical segregated populations, one active during vergent motion and swimming and two that are active during left or right rotational motion and swimming. Concerning the longstanding debate about circuits dedicated to vergent and rotational movements, our work favors the Hering hypothesis by showing that separate populations become active during these two distinct behavioral modules.

RESULTS

Uncorrelated motion stimuli cause swimming bouts and decoupled eye movements

Larvae were presented with motion stimuli designed to induce independent horizontal movements of the left and right eyes. Stimuli consisted of a rotating striped pattern projected onto a screen below the head-restrained fish. We divided the screen into two hemifields, and the velocity of the projected gratings was modulated independently in the left and right hemifields (Figures 1A and S1A; Video S1). In this way, stimuli delivered to the two eyes were, on average, uncorrelated. To decouple eye position and velocity, the rotation of the grating was modulated with steps of constant velocity (see STAR Methods; Figure 1A). Five different grating velocities were presented to each eye (−30°/s, −15°/s, 0°/s, 15°/s, and 30°/s), resulting in 25 different stimulus combinations; each of these combinations was presented for 5 s. The stimuli were presented in pseudo-random order and formed a stimulus set that lasted 125 s and was repeated 90–120 times.

While the fish were presented with the stimuli, we tracked eye and tail behavior at 100 and 700 Hz, respectively, using a high-speed camera. Eye and tail positions were extracted, and eye velocities were estimated from changes of the eye positions (see STAR Methods; Figure 1A).

Rather than using coordinates related to the left and right eye, we used coordinates based on "vergence" and "rotation" axes, which result from adding or subtracting the corresponding left and right variables (a simple rotation of the coordinate system; see white axes in Figure 1Bi). Along the vergence axis, stimulus gratings on both halves are then moving either forward (converging) or backward (diverging), mimicking translational

---

Figure 1. Split motion stimuli are used to decouple eye movements

(A) Schematic of visual stimulation (center). Eye rotations are elicited by rotating radial patterns, split into two hemifields, and projected onto a screen placed below the fish (see Video S1). Both eye and tail positions are tracked during stimulus viewing.

(B) (i) Left and right eye positions are decorrelated when using a split stimulus (left, uncorrelated velocity steps). In comparison, they are highly correlated when using a whole-field rotating grating (right, congruent rotation). (ii) Vergence index for fish presented with split, incongruent motion stimuli (8 fish) and congruent rotation stimuli (5 fish). Filled circles, mean across fish. Open circles, individual fish.

(C) Eye velocity is modulated by stimulus velocity (see also Figure S1). (i) Left eye and right eye velocities (saccades removed) for each stimulus velocity presented on the ipsilateral side of the screen. Red and blue points, mean across fish (N = 8); gray traces, individual fish. The slope of the fitted lines reflects the eye velocity gain, i.e., the modulation of eye velocity by stimulus velocity. (ii) Eye velocity gain, pooled for both eyes, for stimuli grouped into rotating and vergent. Filled circles, mean across fish (n = 8). Open circles, individual fish (see STAR Methods and Figure S1D).

(D) Swimming bout type is modulated by stimulus category (see also Figure S1A). Filled circles, mean across fish (n = 8). Open circles, individual fish. Conv, converging; Div, diverging; LRot, leftward rotation (counterclockwise); RRot, rightward rotation (clockwise).
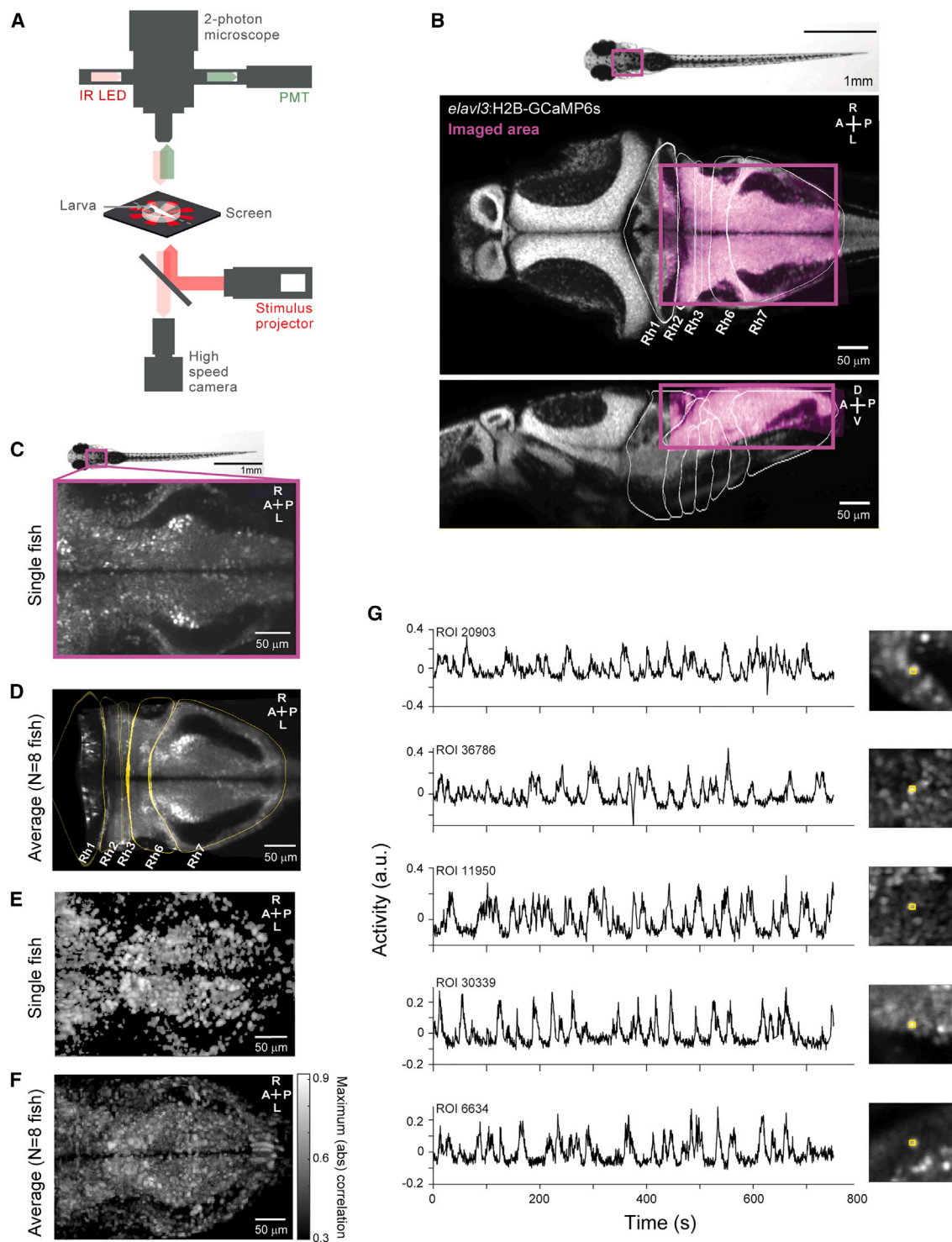
See also Figure S1 and Video S1.

Figure 2. Activity related to behavior is widespread in the zebrafish hindbrain

(A) Schematic of experimental setup (see STAR Methods), showing simultaneous brain imaging, behavior monitoring, and visual stimulus presentation.

(B) Representative plane highlighting the imaged region (magenta) overlaid on the corresponding plane of the Z-brain atlas.[47] Top, dorsal view. Bottom, sagittal view.

(C) Example plane of the imaged area in a representative fish.

(D) Example plane of the average image stack across eight fish (see STAR Methods).

(E) Maximum absolute correlation value with any of the expanded set of behavioral regressors (see STAR Methods) for an example fish (maximum projection of the imaged stack).

(legend continued on next page)

motion. Similarly, eye positions and velocities are converging or diverging. Along the rotation axis, stimulus gratings on both halves are moving either toward the left (counterclockwise) or toward the right (clockwise), thereby mimicking rotational motion (Figure S1A). Similarly, eyes move conjugately either in clockwise or counterclockwise directions.

Whereas congruently rotating stimuli drove the eyes to rotate (Figure 1Bi, right), uncorrelated velocity steps drove the eyes to explore various rotation and vergence states (Figure 1Bi, left). To quantify the difference in prevalence of vergence positions, we defined a "vergence index" (see STAR Methods; Figure 1Bii). This index was higher when fish were presented with incongruently rotating gratings, as compared with fish presented with congruently rotating gratings. Convergent eye positions, usually observed during prey capture,[43] were readily driven with the stimuli used here, namely during the presentation of back-to-front stimuli to both eyes. Divergent eye positions were, on the other hand, underrepresented; this is consistent with the observation that fish species with yoked eye movements show reduced or absent responses to front-to-back whole-field motion.[44,45] The velocity of either eye increased linearly with the velocity of the stimulus in the corresponding hemifield (Figures 1Ci, S1B, and S1C). However, the gain with which eye movements were modulated was not equal across stimuli: fish tracked rotating stimuli with higher gain than vergent stimuli (Figures 1Cii and S1D).

Eye movements were accompanied by tail flicks, which could be classified as left and right turns, and forward swims[40] (see STAR Methods). Forward swims occurred mostly when fish were presented with vergent stimuli moving back-to-front (converging), which resemble forward translational flow (Figures 1D, S1A, and S1E). Turns occurred less frequently (not shown), but their directionality was determined by the stimulus: overall, left rotating stimuli drove turns to the left while right rotating stimuli drove turns to the right (Figures 1D and S1E).

Hindbrain activity is highly correlated with eye and stimulus variables

To understand the role of the hindbrain in this stimulus-driven oculomotor behavior, we recorded hindbrain activity in 5- to 7-day-old larvae expressing GCaMP6s in the nuclei of most neurons (*Tg(elavl3:Hsa.H2B-GCaMP6s)* jf5Tg[46]), using a two-photon microscope with an imaging rate of 2 Hz (see STAR Methods; Figures 2A–2D). We simultaneously presented the uncorrelated motion stimuli and monitored the larval behavioral response. We targeted the dorsal aspect of the intermediate and inferior medulla oblongata, spanning rhombomeres 2–7 in the hindbrain. For each larva (n = 8 larvae), we imaged a stack of 80–110 planes in 1-μm steps. For each plane, the 25 stimulus combinations were presented in a randomized order before advancing to the next plane, resulting in an imaging time of 125 s per plane. Fish showed sustained behavioral responses throughout the imaging session (Figure S1B).

Activity, measured as fluorescence changes in regions of interest (ROIs), was extracted from the imaging data after preprocessing (see Figure 2G, Video S2, and STAR Methods). Briefly, data were first motion corrected and then segmented by dividing each hindbrain stack into cuboid-shaped ROIs. The resulting ROIs were overlapping and tiled the whole imaged area. We then sought to characterize the relationship between the neural activity and the experimental and behavioral variables. The complete set of the 12 "original" variables used is shown in Figure S2A.

Neuronal activity could, in principle, be explained not only by the *present* state of the behavior/stimulus variables but also their *past* or *future* state (the latter, for instance, for activity that would predict a motor command). Indeed, the dynamics of the Ca indicator alone introduce a dependence of current neuronal activity onto future measurements. To account for any dependencies on past or future states, we built a set of additional "shifted" variables: each original variable was shifted by up to 20 s into the past and 10 s into the future (see STAR Methods).

We first correlated activity to our regressors as well as various thresholded variants and combinations of them (STAR Methods; Table S1). This approach has proven useful to reveal areas active during a given behavior.[26,38,42] Regressor-activity correlations were widespread in the hindbrain: a large population of ROIs was highly correlated with at least one of the stimulus and behavioral variables included in the analysis (Figures 2E and 2F). However, many individual ROIs correlate with *both* sensory and motor variables (not shown; see also Portugues et al.[38]). Since regressors are correlated with each other to some degree, this mixing of sensory and motor variables in neural activities may simply reflect such latent correlations rather than a true correlation of the neural activities with the respective sensory and motor variables. To investigate how ROI activity could be explained by our set of regressors, we turned to multiple linear regression (MLR).

Hindbrain activity can be explained by a low-dimensional set of features

Classical MLR finds for each ROI a set of weights that explains the activity of that ROI as a function of the regressors (Figures 3A and S3A). As described above, our shifted regressors covered time windows in the past and future. For a given ROI, we can then find a linear combination of the shifted regressors, that is, a pattern of weights, that explains the activity of the ROI as a function of the original variables and their time shifts (Figure 3A). The shifted weights of each original variable can be represented as a kernel (see inset in Figure 3A), where negative shifts reflect how past states of the variable influence activity, and positive shifts reflect how future states of the variable influence activity. This kernel will also reflect the dynamics of the Ca indicator.

However, classical MLR has two downsides. First, by analyzing each ROI individually, we are not truly leveraging the size of the data to discover activation patterns spread across

---

(F) Average maximum absolute correlation maps across eight fish, after registration to an internal template (see STAR Methods; maximum projection of average stack). Correlation maps are thresholded at 0.3 absolute correlation value.

(G) Example traces of ROIs used in the analysis.
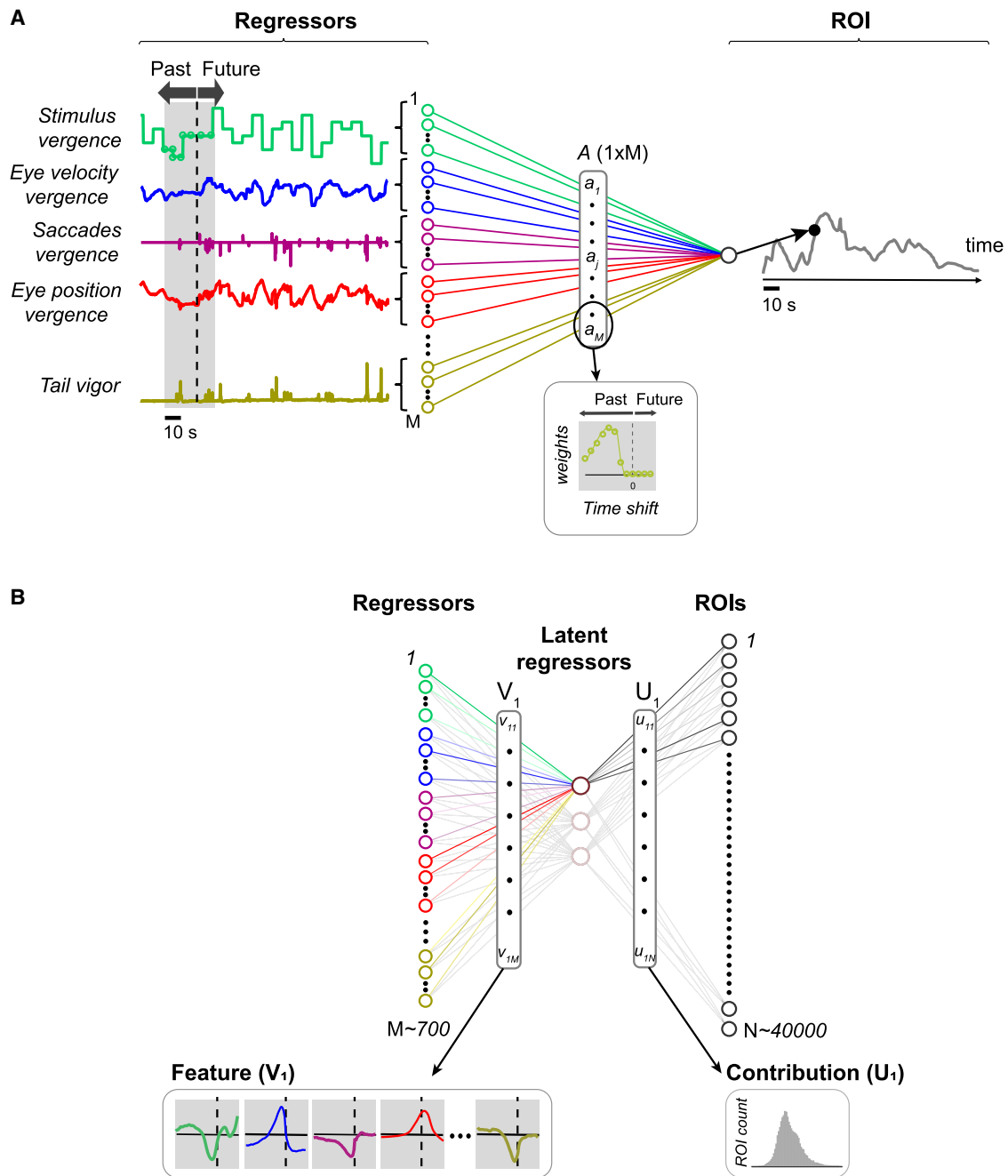
See also Table S1, and Video S2.

Figure 3. Regression models

(A) Multiple linear regression model for a single ROI. For each original variable (only a subset shown here, see Figure S2), the regression model finds a set of weights that corresponds to the contribution of the variable at different time points (gray window, left) to ROI activity at the present time point (black dot, right). Inset shows the weights for one of the variables. Dotted line corresponds to no time-shift.

(B) Reduced-rank regression. Each time-shifted regressor is first mapped onto a set of latent regressors. The pattern of weights (V_1) that determines the mapping for one latent regressor is called a *feature* (left inset, each regressor is represented in one color). In turn, the latent regressor is associated with a pattern of ROI activity, determined by its contribution weights (U_1). Right inset shows distribution of the U_1 values (U_1 contribution) for this example feature. This distribution illustrates how strongly the latent regressor associated with this feature is expressed across the population.

See also Figures S2 and S3.

the whole population. Second, it is not immediately clear how to interpret the weights found by MLR succinctly. We therefore turned to reduced-rank regression (RRR),[48] a variant of MLR

which enforces a rank constraint on the matrix of weights and has proven useful in the analysis of neural populations.[32,49,50] Whereas classical MLR finds for each ROI a separate mapping
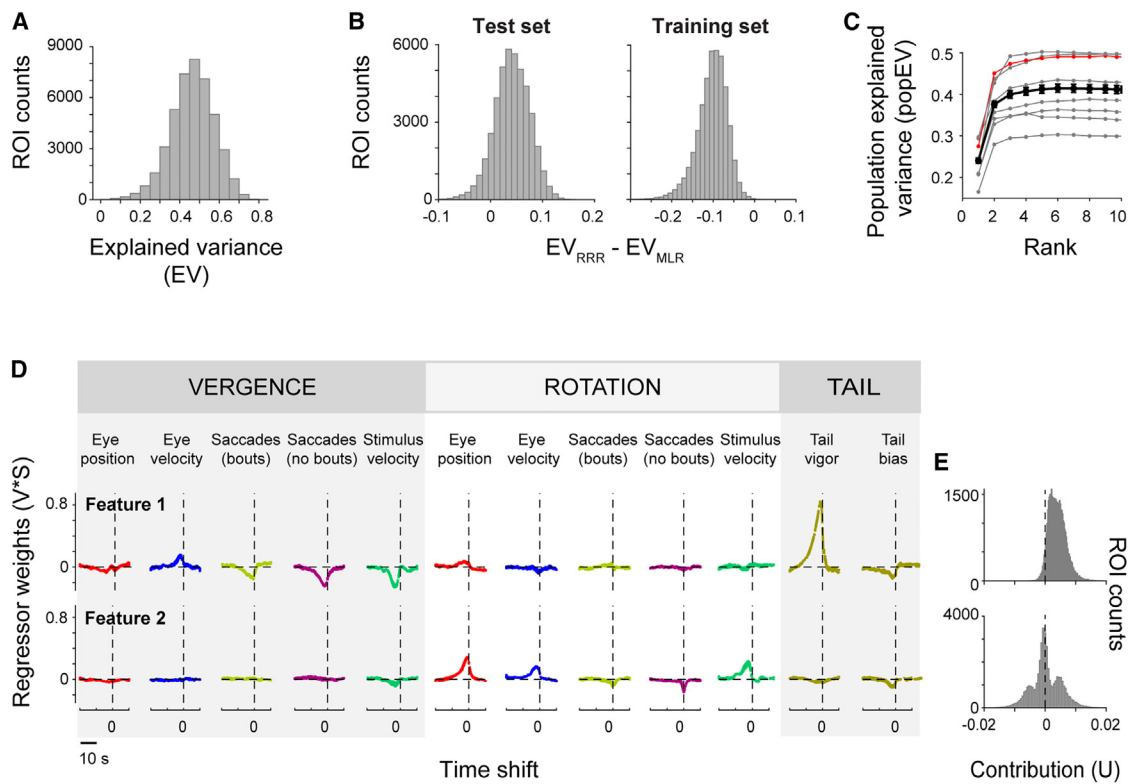
Figure 4. Activity is explained by a small number of features that separate vergence and rotation variables

(A) Explained variance (EV; cross-validated) for the ROIs of an example fish using RRR.

(B) The cross-validated explained variance of the best RRR model (EV_{RRR}) was generally higher than the explained variance of the best MLR model (EV_{MLR}) (left). Right shows performance on training data, i.e., without cross-validation. Same fish as in (A).

(C) Population-explained variance (popEV, cross-validated; see STAR Methods) as a function of the number of features (rank) included in the model for each individual fish (gray traces; example fish in A and B is shown in red) and across fish (average of 8 fish, black trace; error bars correspond to SEM).

(D) The first two features for the example fish. Feature traces are scaled by their overall importance (V*S; see STAR Methods). For each feature, variables are color-coded and sorted into vergence, rotation, and tail variables. Vertical dotted line indicates a time shift of zero. Traces of five cross-validation runs are shown and closely overlap. Note that feature 1 groups activity related to vergence and swimming, whereas feature 2 groups activity related to rotation. Features 3–6 of this fish have only a minor contribution to the popEV (see Figure S5).

(E) Contribution of the latent regressors associated with features 1 (vergence) and 2 (rotation) to ROI activity for the same example fish (43,622 ROIs).

See also Figures S4 and S5.

from the regressors to the ROI activity (Figures 3A and S3A), RRR first finds a low-dimensional subspace of *latent* regressors, i.e., a small set of latent variables, and then finds, for each ROI, a separate mapping from the latent regressors to the ROI activity (STAR Methods; Figure S3B). Formally, the latent regressors are linear combinations of the original regressors, and we will refer to the respective combination of weights as *features*. In turn, the activity of each ROI is explained by a specific, linear combination of these latent regressors, and we will refer to these weights as the *contributions* of the latent regressors to the ROIs (Figures 3B and S3B). Thus, a feature corresponds to a pattern of regressors that, whenever present, gives rise to a particular pattern of ROI activities (Figure 3B). Since our regressors are time-shifted, each feature is composed of a set of "kernels" (inset in Figure 3B), and each kernel contains the weights of one original regressor at different time points in the window analyzed.

We built separate RRR (as well as MLR) models for eight fish, including 732 regressors (12 original regressors plus their shifts)

and 26,000–57,000 ROIs (median 45,588 ROIs/fish; see STAR Methods). The models were regularized and cross-validated (STAR Methods). Figure 4 shows the results for an example fish. For this fish, the best model had rank 6, i.e., six latent regressors were sufficient to explain the activity of a population of 43,622 ROIs. The performance of the selected model, measured as explained variance (see Figure 4A; STAR Methods), was estimated for each individual ROI. The mean explained variance in the test set was 0.46, with some ROIs having explained variance as high as 0.76 (Figures 4A and S4D; note that the mean predictive power depends on the criterion used to include ROIs in the model; see STAR Methods).

We next asked whether the dimensionality reduction step inherent to RRR gains explanatory power for some ROIs at the cost of losing explanatory power for others. Such a tradeoff could occur when the features, which capture only a subspace of the full regressor space, are ill-matched for some (outlier) ROIs. We therefore compared the performance of the RRR and the full MLR models for individual ROIs, using the optimal

regularization parameter for each model. For almost all ROIs, predictive power in the test set was higher for the RRR model than the MLR model (Figure 4B, left), and we found no evidence for clear outliers. Note that for the training set the MLR model performed better, as expected (Figure 4B, right). Thus, the latent regressors found by the RRR model capture as much variance as possible given the visual stimuli, the measured behavioral variables, and the imaging noise.

For the example fish, the first two latent regressors contributed to almost all (92%) of the population explained variance. Even though across fish the best models had between three and six latent regressors, on average, only little explanatory power was gained by the model when including more than two latent regressors (Figure 4C). Using RRR, we therefore greatly shrank the complexity of the problem and revealed an effectively two-dimensional subspace of regressors that captures a substantial fraction of hindbrain population activity. This strong drop in dimensionality could not be explained by correlations among the regressors, as the regressor space had many more dimensions (Figures S2D and S2E). For the rest of the analysis, we therefore focused on the first two latent regressors.

Hindbrain activity is largely explained by rotation and vergence features

As described above, each latent regressor is generated through a pattern of regressor weights or feature (Figures 3B and S3B). Figure 4D shows the first two features for the example fish (all six features of the model can be found in Figure S5). Each feature decomposes into a set of kernels, one for each original regressor. The half-decay time of the kernels (median = 4.01 s) roughly reflects the expected decay time of the Ca indicator. The first feature is almost exclusively composed of kernels associated with vergence regressors (Figure 4D, top row). These regressors include the stimulus vergence (mimicking translational motion) and the vergent eye velocities. In addition, the first feature also consists of tail vigor, which essentially measures forward swimming. This feature therefore combines sensory and motor information. The second feature, on the other hand, is exclusively made of rotation regressors—again including sensory (stimulus rotation) and motor information (rotation of the eyes, both in terms of eye position and eye velocity). Thus, the two features that contribute the most to explaining population activity in our model seem to separate vergence and rotation information. In what follows, we will refer to them as *vergence* and *rotation* features, respectively. We note that saccade-related activity was only observed in the vergence feature and that tail bias, which reflects the laterality of the tail flick, was noticeable in both features.

When we built models for eight different fish, we found similar vergence and rotation features in all of them (not shown). In six out of eight fish, the vergence and rotation features corresponded to the first two features; in the two remaining cases, vergence and rotation features could be identified among the first three features of the model.

ROIs cluster into three groups in feature space

We next asked how the latent regressors contribute to the activity of each ROI by plotting the distributions of their contribution values U (see STAR Methods; Figure 3B). The latent regressor associated with the vergence feature showed an asymmetric contribution to ROI activity: for the vast majority of ROIs, contributions were positive (Figure 4E, top row). The latent regressor associated with the rotation feature, on the other hand, showed three peaks: a central peak, indicating no contribution of this feature, and two symmetric peaks, indicating positive or negative relations of ROIs with this latent regressor (Figure 4E, middle row). Accordingly, different ROIs are active during leftward or rightward rotations, respectively.

To better understand the nature of these three peaks, we studied the joint contribution of the latent vergence and rotation regressors to ROI activity (Figure 5A) and found that ROIs form three main groups in all fish. We therefore assigned ROIs to clusters, using either manual or automatic clustering methods. As shown for an example fish in Figures 5B and 5C, we drew a polygon around the clusters and assigned ROIs accordingly. Using unsupervised clustering in multiple dimensions (Cluster Dv[51]), the same three clusters were found (Figure 5D). The asymmetry we observed in the contribution of the latent vergence regressor (U_1) is also evident here: all clusters have a positive contribution of the latent vergence regressor. Similarly, the three bumps observed in the distribution of feature 2 contributions (U_2) are evident in the density plots: the central peak maps to the green cluster, while the positive and negative peaks map to the red and blue clusters.

We note that in some fish, these clusters can likely be further subdivided: in at least two of the fish (fish 1 and 5), one can see a further subdivision of one of the clusters; this was not further investigated, as the clustering algorithm was unable to separate them. Thus, ROIs in the hindbrain form three principal groups according to how the latent vergence and rotation regressors contribute to their activity.

The three clusters represent vergence, leftward rotation, and rightward rotation

To understand what these three clusters represent, we examined a representative point of each cluster, its centroid. For each centroid, we visualized the regressor weights that result from combining the relevant features (Figure 6). The centroid of cluster 1 (green) contains mostly contributions of vergent variables, including stimulus velocity and eye velocity as well as swimming. ROIs in this cluster will be active whenever the fish is presented with vergent stimuli and engaged in a vergent movement of the eyes and swimming. We will therefore refer to this cluster as the *vergence cluster*. Because stimulus and (low) eye velocity appear with opposite signs, consistent with a representation of retinal slip, we hypothesize that ROIs in this cluster could represent information related to translational optic flow. Interestingly, convergent stimuli (which resemble forward translational flow) elicit swimming (see Figure 1D), which is also represented in this cluster.

The centroids of clusters 2 (red) and 3 (blue), on the other hand, are dominated by rotational variables, suggesting that ROIs in these clusters are related to rotational flow, either counterclockwise (red cluster, positive contribution of rotation variables) or clockwise (blue cluster, negative contribution of rotation variables). We will therefore refer to these clusters as the *leftward (counterclockwise) rotation cluster* and *rightward (clockwise) rotation clusters*, respectively. We note that the contribution of
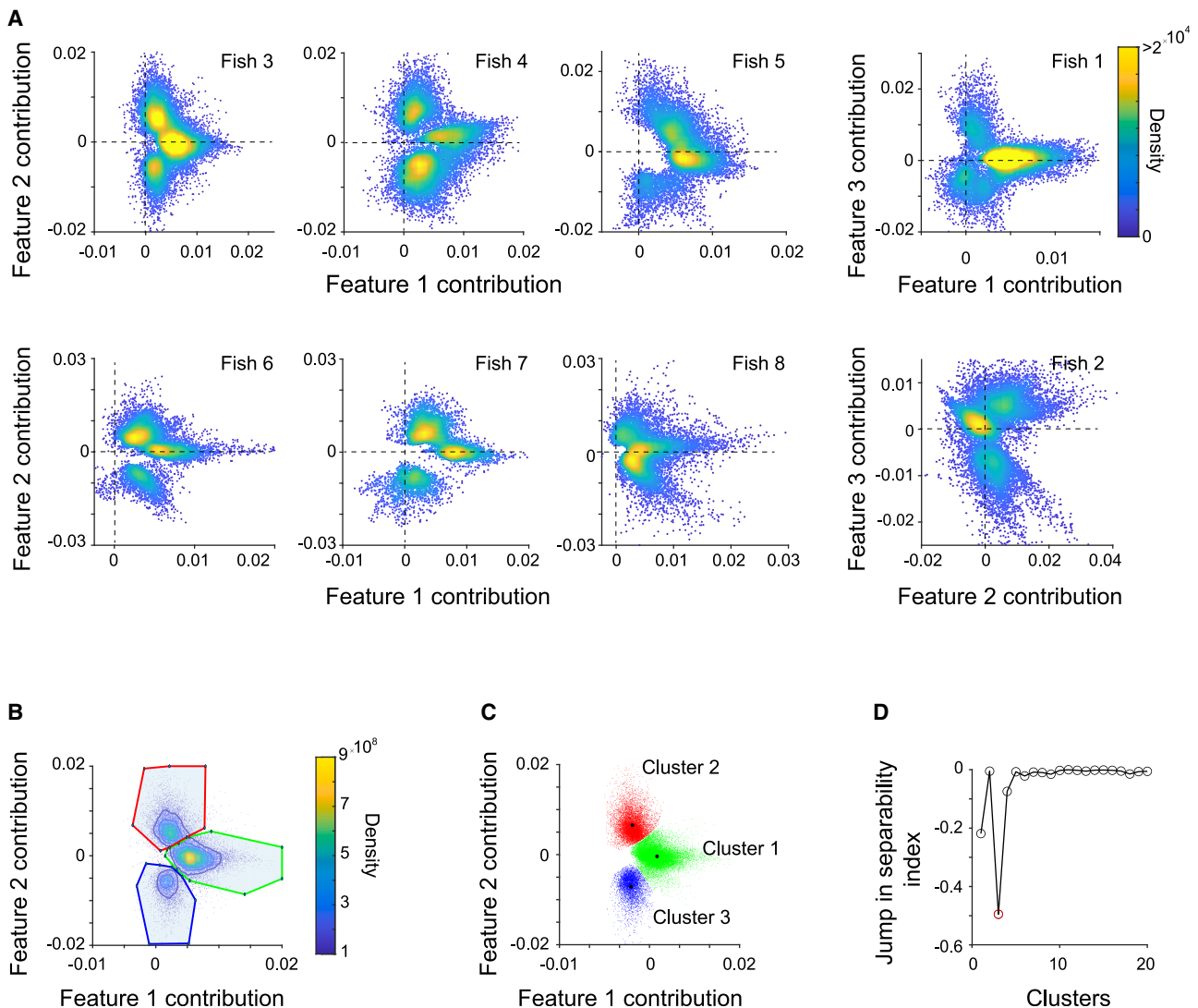
Figure 5. Equivalent ROI clusters are found across all imaged fish

(A) Contributions (U) to ROI activity of latent regressors associated with vergence and rotation features group into three clusters. Each dot corresponds to an ROI, each panel to a different fish. Only ROIs with EV > 0.4 are included.

(B) Manual assignment of ROIs to three clusters in feature contribution (U_1-U_2; see STAR Methods) space for an example fish (STAR Methods based on the density plot.

(C) ROIs for the example fish are color-coded according to their cluster assignment (ROIs are subsampled here for better visualization). Black asterisks mark cluster centroids.

(D) Using ClusterDv[51] (see STAR Methods) we also find three clusters.

tail bias (whose strength was somewhat variable across fish) was consistent with the behavioral observations: leftward rotating stimuli elicited preferably a left turn (Figure 1E). Accordingly, ROIs active during leftward rotations (leftward rotation cluster, red) showed activity related to left turns (note that a negative bias corresponds to a left turn; see STAR Methods). The reverse is true for rightward turns.

ROIs in each cluster are spread around the centroid. In the rotation clusters, this spread reflects a varying contribution of the vergence (feature 1) variables (Figure 5C). For eye and stimulus velocity, ROIs thereby ranged from representing bilateral eye and stimulus velocity rotation to representing ipsilateral

eye yet contralateral stimulus velocity rotation (albeit in ipsiversive direction; Figures S6A–S6C). The representation of eye position was simpler and did not change much across the cluster, with both clusters representing conjugate eye position (Figures S6B and S6C).

ROIs in different clusters correspond to separate anatomical populations

To visualize the anatomical distribution of ROIs belonging to these clusters, we built spatial maps where we color-coded each ROI according to its cluster membership (Figure 7). ROIs in the vergence cluster were colored green and ROIs
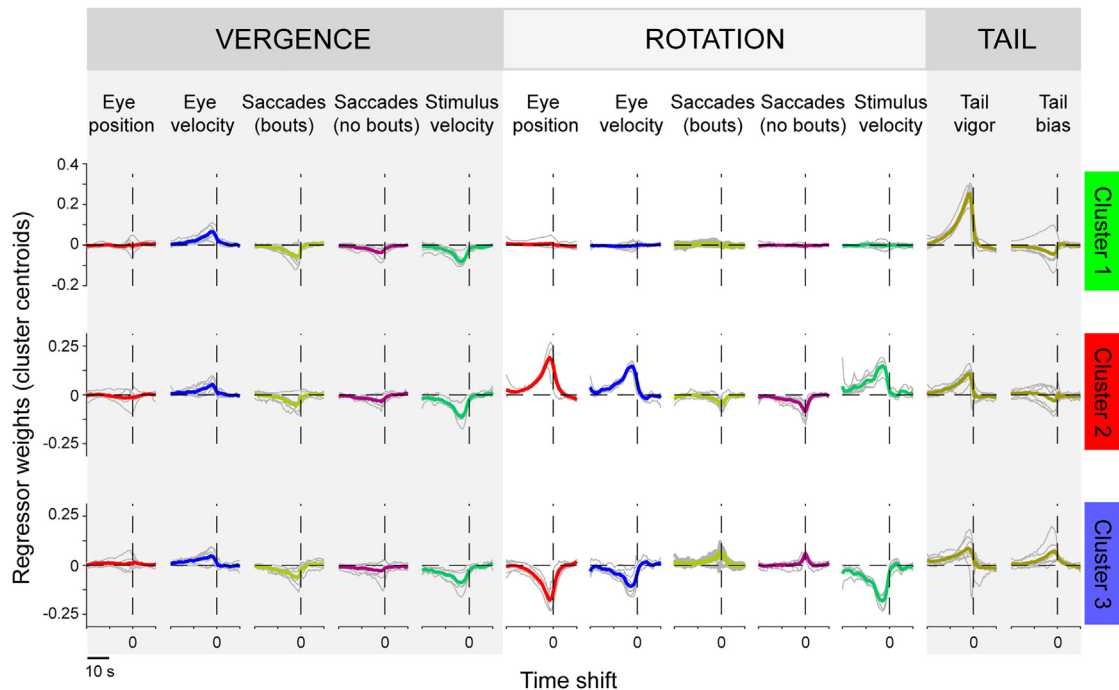
Figure 6. Clusters relate to vergence and left/right rotational motion

The weighted contribution of features 1–3 is shown for each cluster's centroid. Each row corresponds to a cluster, and variables are grouped into vergence, rotation, and tail variables (compare to Figure 4D). Cluster 1 (green) is composed exclusively of vergence variables and swimming. Clusters 2 (red) and 3 (blue) relate to leftward and rightward rotation, respectively. Gray traces, individual fish. Color traces, mean across seven fish (one fish was excluded here because the tail tracking was too noisy).

See also Figure S6.

in the leftward and rightward rotation clusters were colored in red and blue, respectively. We found that clusters were spatially segregated, with the rightward and leftward rotation clusters symmetrically localized to the right and left hemispheres, respectively, while the vergence cluster was distributed across both hemispheres. The rotation clusters were distributed in more compact areas, whereas the vergence cluster was more widely distributed. Across fish, the anatomical organization of the clusters was similar (Figures 7B and S7; Video S3).

The three clusters spanned the whole imaged area, which corresponded to the dorsal aspect of the intermediate and inferior medulla oblongata. The clusters did not clearly overlap with any of the annotated hindbrain nuclei (mapzebrain[52], Z-brain), except for some overlap with the facial motor nucleus and some overlap of ROIs in the vergence cluster with the medial octavolateralis nucleus and, more prominently, with the vagal sensory lobe and vagus motor nucleus (mapzebrain atlas). In addition, we did find some overlap with some molecularly defined areas. The vergence cluster overlapped with neurons in the Z-brain 6.7FDhcrtR-Gal4 stripe 1, neurons expressing Gad1b (Gad1b stripes 1 and 2, Z-brain) and, more prominently, neurons expressing Ptf1a (Ptf1a stripe, Z-brain). Neurons in the rotation clusters also overlapped with the Z-brain 6.7FDhcrtR-Gal4 cluster 1. Neurons in these clusters also mapped to regions expressing Gad1b (Gad1b stripe 3, Z-brain) and, more prominently, to areas expressing the glycinergic transporter (Glyt2 cluster 1, and stripes 1–3, Z-brain), Otpb and Ptf1a. These anatomical overlaps provide some hints to the neurotransmitter identity of the neurons belonging to our functional clusters.

Thus, our analysis shows that, during rotational and vergent eye movements, two different populations in the dorsal medulla are active. One population relates to translational motion while the other relates to rotational motion. Notably, the anatomical left/right asymmetric distribution of the ROIs in the rotation clusters was consistent with previously described representation of ipsiversive movements in the hindbrain.[18,20,25,38,42]

DISCUSSION

Here, we have studied hindbrain activity in zebrafish larvae performing eye and tail movements in response to a sequence of conjugate and disconjugate optokinetic stimuli. Using RRR, we found that a large fraction of population activity in the hindbrain can be explained by two linear combinations of regressors, which we called latent regressors. Based on the contribution of these latent regressors to ROI activity, ROIs formed three main clusters. These clusters grouped ROIs whose activity represented vergent eye movement and swimming (1), and conjugate eye movement in clockwise (2) and counterclockwise (3) directions, as well as swimming. ROIs belonging to the three clusters showed a spatial distribution that was conserved across fish, suggesting that translational and rotational behaviors are encoded in separate circuits.

Neurons tuned to (horizontal) eye position and velocity have been extensively studied in various motor nuclei, particularly
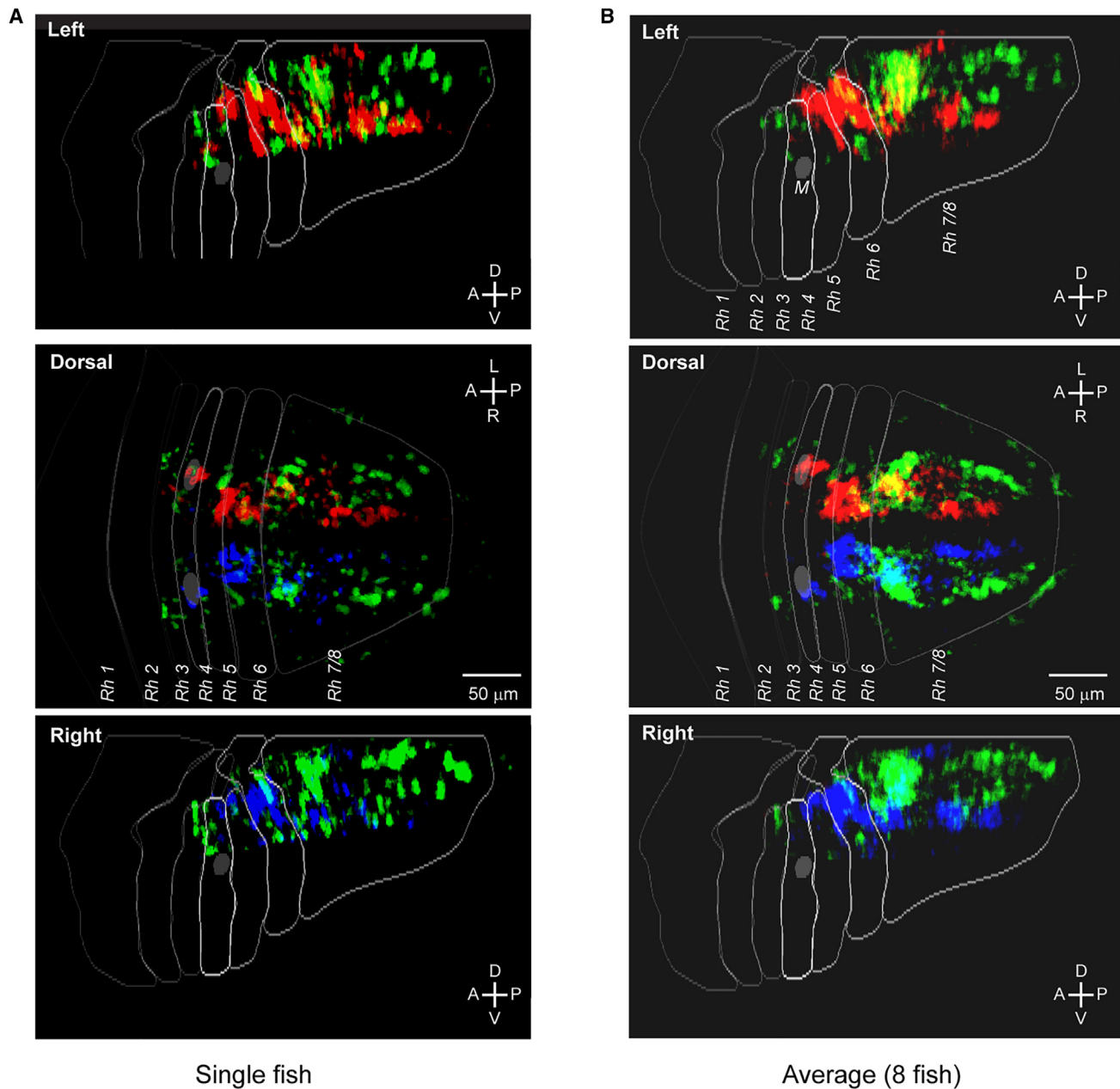
Figure 7. Anatomical distribution of ROIs belonging to the vergence and rotation clusters

(A) Spatial distribution of the ROIs assigned to the three clusters in the example fish (32,228 ROIs with EV > 0.4).

(B) Average distribution of the ROIs assigned to the three clusters (n = 8 fish). Individual maps (see Figure S7) were registered to the Z-brain template before averaging. Scale bar, 50 μm. Dark gray ellipse shows the location of the Mauthner cells (M). Rhombomere contours and Mauthner cell correspond to Z-brain masks.[47]

See also Figure S7 and Video S3.

in primates[53,54] and goldfish[55] and more recently in zebrafish.[18,56–58] The surveyed brain regions include the abducens and oculomotor nucleus, which directly innervate the muscles that move the eyes,[13,16,17,53,54,59] as well as the oculomotor integrator, a brain area that transforms velocity commands into eye position.[17,55–57,60–63] In a whole-brain study,[38] we showed that activity correlated with eye position, eye velocity, and swimming was widely distributed across the brain. Compared with previous studies,[15,18,19] our present work focuses on more dorsal areas of the hindbrain (but see Leyden et al.[20]).

Even though the majority of responses in motor nuclei are monocular, there is a substantial fraction of neurons that represent eye movements binocularly.[15,18–20] Here, we show that eye position representations are bilateral (conjugate), whereas the velocity signals span a continuum from binocular to monocular representation. In a recent study,[18] a spatial gradient of

binocular/monocular activity was described in ventral areas of the zebrafish hindbrain; however, we did not find such a clear spatial organization (data not shown) in the more dorsal areas. Interestingly, our results suggest that velocity-encoding neurons appear distributed across the hindbrain and are also sensitive to eye position (see also Brysch et al.[18]); this is different from the adult goldfish, where a nucleus solely encoding eye velocity was found.[64]

The neurons we imaged display a variety of tuning to eye position, velocity, and saccades, as well as tail movements, as shown by correlation maps (Figure 2; maps for individual regressors not shown, but see Portugues et al.[38]). This apparent complexity at the single-neuron level essentially disappears when using RRR, which can be thought of as multivariate regression with built-in dimensionality reduction. Using RRR leverages the size of the data and identifies features that are common in the population, even if they are contaminated by imaging noise. Neural activity was dominated by two modes of population activity that combined eye and tail movements. In turn, the diversity of tuning observed in our data at the single-neuron level stems from different neurons expressing different combinations of these population modes (Figure S6) as well as imaging noise. Indeed, responses in our rotation clusters are diverse and fall in a continuum, going from monocular to conjugate (binocular) tuning of eye velocity.

We find a clear organization of the neurons into three different, anatomically separated groups. ROIs belonging to the rotation clusters were symmetrically distributed across the midline and represented ipsiversive motion/position, as previously observed for eye and tail movements.[22–25,38] The clusters mix sensory and motor variables, suggesting that they are involved in sensorimotor transformations that segregate translational optic flow, vergent movement of the eyes, and forward swims from rotational optic flow, conjugate eye movements, and (potentially) turning bouts. This is consistent with a role for the hindbrain in sensorimotor transformation, as previously postulated.[22,24,40]

That neuronal activity in this area can be assigned to two different principal modes, one related to rotational (conjugate) motion and one related to translational (vergent) motion, is consistent with a binocular organization of the control of eye movements, as postulated by Hering,[9,10] at least in the areas imaged here. However, it is important to note that, in the rotational clusters, responses showed a gradient from binocular to monocular encoding of eye velocity (but not position). The monocular responses observed in downstream areas (oculomotor integrator, abducens nucleus) could reflect a combination of conjugate and vergence signals provided by the neurons imaged here or could be directly informed by the subpopulation displaying monocular responses.

One potential caveat here is that the regression method may have failed to separate the (highly correlated) stimulus and eye velocities. Theoretically, regularized MLR will separate correlated variables (assuming correlations smaller than one and sufficient data given the noise level). However, if the relation between regressors and behavioral variables is non-linear, then such a separation is not guaranteed. Moreover, the eye velocity regressor, which is estimated from noisy eye positions, is less reliable than the stimulus velocity regressor, such that its overall importance for ROI activity may have been underestimated. In

turn, it is possible that the vergence cluster is, in truth, really related to retinal slip (note that fish tracked stimuli with low gain, particularly vergent stimuli; see Figure 1Cii), whereas the rotation cluster is only related to eye velocity. In addition, we cannot rule out that responses occurring at timescales faster than that of the Ca indicator may have been missed. Future experiments will be able to resolve these questions.

In summary, we show here that by using RRR, which combines dimensionality reduction with multilinear regression analysis, we could leverage large datasets to reveal the dominant modes of behavior-related activity present in the hindbrain population we imaged. We found that a large fraction of hindbrain activity, when responding to different patterns of whole-field rotation, was distributed in three populations of neurons, representing translational and left/right rotational information. This method can be useful to reveal the main modes of population activity and reduce the complexity of datasets in large-scale recordings in behaving animals.

STAR★METHODS

Detailed methods are provided in the online version of this paper and include the following:

- KEY RESOURCES TABLE
- RESOURCE AVAILABILITY
  - Lead contact
  - Materials availability
  - Data and code availability
- EXPERIMENTAL MODEL AND STUDY PARTICIPANT DETAILS
  - Fish care
- METHOD DETAILS
  - Calcium imaging and behavior recording
  - Visual stimulation
  - Behavior tracking
  - Anatomical registration
- QUANTIFICATION AND STATISTICAL ANALYSIS
  - Behavior analysis
  - Image analysis
  - Data dimensionality
  - Correlation analysis
  - Regression analysis
  - Clustering
  - Monocularity index

SUPPLEMENTAL INFORMATION

Supplemental information can be found online at https://doi.org/10.1016/j.cub.2023.08.037.

AUTHOR CONTRIBUTIONS

C.E.F., M.B.O., and R.P. conceived the experiments. C.E.F., M.H.M.d.G., and R.P. performed the experiments. C.E.F. and C.K.M. conceived the analysis. C.E.F. analyzed the data. A.L. developed the behavioral tracking software. A.D.O. performed brain registrations. C.E.F. and C.K.M. wrote the manuscript. All authors provided feedback on the manuscript.

DECLARATION OF INTERESTS

The authors declare no competing interests.

INCLUSION AND DIVERSITY

We support inclusive, diverse, and equitable conduct of research.

REFERENCES

1. Brockerhoff, S.E., Hurley, J.B., Janssen-Bienhold, U., Neuhauss, S.C., Driever, W., and Dowling, J.E. (1995). A behavioral screen for isolating zebrafish mutants with visual system defects. Proc. Natl. Acad. Sci. USA *92*, 10545–10549. https://doi.org/10.1073/pnas.92.23.10545.

2. Collewijn, H. (1969). Optokinetic eye movements in the rabbit: input-output relations. Vision Res. *9*, 117–132. https://doi.org/10.1016/0042-6989(69)90035-2.

3. Easter, S.S., and Nicola, G.N. (1996). The development of vision in the zebrafish (Danio rerio). Dev. Biol. *180*, 646–663. https://doi.org/10.1006/dbio.1996.0335.

4. Krauzlis, R.J. (2013). Eye movements. Chapter 32. In Fundamental Neuroscience, Fourth Edition, L.R. Squire, D. Berg, F.E. Bloom, S. du Lac, A. Ghosh, and N.C. Spitzer, eds. (Academic Press), pp. 697–714. https://doi.org/10.1016/B978-0-12-385870-2.00032-9.

5. Collett, T.S. (1980). Angular tracking and the optomotor response an analysis of visual reflex interaction in a hoverfly. J. Comp. Physiol. *140*, 145–158. https://doi.org/10.1007/BF00606306.

6. Neuhauss, S.C.F., Biehlmaier, O., Seeliger, M.W., Das, T., Kohler, K., Harris, W.A., and Baier, H. (1999). Genetic disorders of vision revealed by a behavioral screen of 400 essential loci in zebrafish. J. Neurosci. *19*, 8603–8615. https://doi.org/10.1523/JNEUROSCI.19-19-08603.1999.

7. Orger, M.B., Smear, M.C., Anstis, S.M., and Baier, H. (2000). Perception of Fourier and non-Fourier motion by larval zebrafish. Nat. Neurosci. *3*, 1128–1133. https://doi.org/10.1038/80649.

8. Beck, J.C., Gilland, E., Tank, D.W., and Baker, R. (2004). Quantifying the ontogeny of optokinetic and vestibuloocular behaviors in zebrafish, medaka, and goldfish. J. Neurophysiol. *92*, 3546–3561. https://doi.org/10.1152/jn.00311.2004.

9. Hering, E. (1977). The Theory of Binocular Vision: Ewald Hering (1868) (Springer Science & Business Media).

10. Westheimer, G. (2014). The law of equal innervation of both eyes: Thomas Reid preceded Hering by a century. An historical note. Vision Res. *101*, 32–33. https://doi.org/10.1016/j.visres.2014.04.016.

11. Helmholtz, H.L. (1962). Helmholtz's Treatise on Physiological Optics (Dover).

12. King, W.M. (2011). Binocular coordination of eye movements – Hering's law of equal innervation or uniocular control? Eur. J. Neurosci. *33*, 2139–2146. https://doi.org/10.1111/j.1460-9568.2011.07695.x.

13. Mays, L.E. (1984). Neural control of vergence eye movements: convergence and divergence neurons in midbrain. J. Neurophysiol. *51*, 1091–1108. https://doi.org/10.1152/jn.1984.51.5.1091.

14. Mays, L.E., and Gamlin, P.D. (1995). Neuronal circuitry controlling the near response. Curr. Opin. Neurobiol. *5*, 763–768. https://doi.org/10.1016/0959-4388(95)80104-9.

15. Sylvestre, P.A., and Cullen, K.E. (2002). Dynamics of abducens nucleus neuron discharges during disjunctive saccades. J. Neurophysiol. *88*, 3452–3468. https://doi.org/10.1152/jn.00331.2002.

16. Van Horn, M.R., and Cullen, K.E. (2009). Dynamic characterization of agonist and antagonist oculomotoneurons during conjugate and disconjugate eye movements. J. Neurophysiol. *102*, 28–40. https://doi.org/10.1152/jn.00169.2009.

17. Zhou, W., and King, W.M. (1998). Premotor commands encode monocular eye movements. Nature *393*, 692–695. https://doi.org/10.1038/31489.

18. Brysch, C., Leyden, C., and Arrenberg, A.B. (2019). Functional architecture underlying binocular coordination of eye position and velocity in the larval zebrafish hindbrain. BMC Biol. *17*, 110. https://doi.org/10.1186/s12915-019-0720-y.

19. Debowy, O., and Baker, R. (2011). Encoding of eye position in the goldfish horizontal oculomotor neural integrator. J. Neurophysiol. *105*, 896–909. https://doi.org/10.1152/jn.00313.2010.

20. Leyden, C., Brysch, C., and Arrenberg, A.B. (2021). A distributed saccade-associated network encodes high velocity conjugate and monocular eye movements in the zebrafish hindbrain. Sci. Rep. *11*, 12644. https://doi.org/10.1038/s41598-021-90315-2.

21. Orger, M.B., Kampff, A.R., Severi, K.E., Bollmann, J.H., and Engert, F. (2008). Control of visually guided behavior by distinct populations of spinal projection neurons. Nat. Neurosci. *11*, 327–333. https://doi.org/10.1038/nn2048.

22. Chen, X., Mu, Y., Hu, Y., Kuan, A.T., Nikitchenko, M., Randlett, O., Chen, A.B., Gavornik, J.P., Sompolinsky, H., Engert, F., et al. (2018). Brain-wide organization of neuronal activity and convergent sensorimotor transformations in larval zebrafish. Neuron *100*, 876–890.e5. https://doi.org/10.1016/j.neuron.2018.09.042.

23. Dunn, T.W., Mu, Y., Narayan, S., Randlett, O., Naumann, E.A., Yang, C.T., Schier, A.F., Freeman, J., Engert, F., and Ahrens, M.B. (2016). Brain-wide mapping of neural activity controlling zebrafish exploratory locomotion. eLife *5*, e12741, https://doi.org/10.7554/eLife.12741.

24. Naumann, E.A., Fitzgerald, J.E., Dunn, T.W., Rihel, J., Sompolinsky, H., and Engert, F. (2016). From whole-brain data to functional circuit models: the zebrafish optomotor response. Cell *167*, 947–960.e20. https://doi.org/10.1016/j.cell.2016.10.019.

25. Wolf, S., Dubreuil, A.M., Bertoni, T., Böhm, U.L., Bormuth, V., Candelier, R., Karpenko, S., Hildebrand, D.G.C., Bianco, I.H., Monasson, R., et al. (2017). Sensorimotor computation underlying phototaxis in zebrafish. Nat. Commun. *8*, 651. https://doi.org/10.1038/s41467-017-00310-3.

26. Dragomir, E.I., Ŝtih, V., and Portugues, R. (2020). Evidence accumulation during a sensorimotor decision task revealed by whole-brain imaging. Nat. Neurosci. *23*, 85–93. https://doi.org/10.1038/s41593-019-0535-8.

27. Wohrer, A., Humphries, M.D., and Machens, C.K. (2013). Population-wide distributions of neural activity during perceptual decision-making. Prog. Neurobiol. *103*, 156–193. https://doi.org/10.1016/j.pneurobio.2012.09.004.

28. Jun, J.K., Miller, P., Hernández, A., Zainos, A., Lemus, L., Brody, C.D., and Romo, R. (2010). Heterogenous population coding of a short-term memory

and decision task. J. Neurosci. *30*, 916–929. https://doi.org/10.1523/JNEUROSCI.2062-09.2010.

29. Rigotti, M., Barak, O., Warden, M.R., Wang, X.J., Daw, N.D., Miller, E.K., and Fusi, S. (2013). The importance of mixed selectivity in complex cognitive tasks. Nature *497*, 585–590. https://doi.org/10.1038/nature12160.

30. Fusi, S., Miller, E.K., and Rigotti, M. (2016). Why neurons mix: high dimensionality for higher cognition. Curr. Opin. Neurobiol. *37*, 66–74. https://doi.org/10.1016/j.conb.2016.01.010.

31. Keemink, S.W., and Machens, C.K. (2019). Decoding and encoding (de) mixed population responses. Curr. Opin. Neurobiol. *58*, 112–121. https://doi.org/10.1016/j.conb.2019.09.004.

32. Kobak, D., Brendel, W., Constantinidis, C., Feierstein, C.E., Kepecs, A., Mainen, Z.F., Qi, X.L., Romo, R., Uchida, N., and Machens, C.K. (2016). Demixed principal component analysis of neural population data. eLife *5*, e10989, https://doi.org/10.7554/eLife.10989.

33. Machens, C.K. (2010). Demixing population activity in higher cortical areas. Front. Comput. Neurosci. *4*, 126. https://doi.org/10.3389/fncom.2010.00126.

34. Saxena, S., and Cunningham, J.P. (2019). Towards the neural population doctrine. Curr. Opin. Neurobiol. *55*, 103–111. https://doi.org/10.1016/j.conb.2019.02.002.

35. Ahrens, M.B., Orger, M.B., Robson, D.N., Li, J.M., and Keller, P.J. (2013). Whole-brain functional imaging at cellular resolution using light-sheet microscopy. Nat. Methods *10*, 413–420. https://doi.org/10.1038/nmeth.2434.

36. Kim, D.H., Kim, J., Marques, J.C., Grama, A., Hildebrand, D.G.C., Gu, W., Li, J.M., and Robson, D.N. (2017). Pan-neuronal calcium imaging with cellular resolution in freely swimming zebrafish. Nat. Methods *14*, 1107–1114. https://doi.org/10.1038/nmeth.4429.

37. Migault, G., Plas, T.L. van der, Trentesaux, H., Panier, T., Candelier, R., Proville, R., Englitz, B., Debrégeas, G., and Bormuth, V. (2018). Whole-brain calcium imaging during physiological vestibular stimulation in larval zebrafish. Curr. Biol. *28*, 3723–3735.e6. https://doi.org/10.1016/j.cub.2018.10.017.

38. Portugues, R., Feierstein, C.E., Engert, F., and Orger, M.B. (2014). Whole-brain activity maps reveal stereotyped, distributed networks for visuomotor behavior. Neuron *81*, 1328–1343. https://doi.org/10.1016/j.neuron.2014.01.019.

39. Favre-Bulle, I.A., Vanwalleghem, G., Taylor, M.A., Rubinsztein-Dunlop, H., and Scott, E.K. (2018). Cellular-resolution imaging of vestibular processing across the larval zebrafish brain. Curr. Biol. *28*, 3711–3722.e3. https://doi.org/10.1016/j.cub.2018.09.060.

40. Haesemeyer, M., Robson, D.N., Li, J.M., Schier, A.F., and Engert, F. (2018). A brain-wide circuit model of heat-evoked swimming behavior in larval zebrafish. Neuron *98*, 817–831.e6. https://doi.org/10.1016/j.neuron.2018.04.013.

41. Privat, M., Romano, S.A., Pietri, T., Jouary, A., Boulanger-Weill, J., Elbaz, N., Duchemin, A., Soares, D., and Sumbre, G. (2019). Sensorimotor transformations in the zebrafish auditory system. Curr. Biol. *29*, 4010–4023.e4. https://doi.org/10.1016/j.cub.2019.10.020.

42. Miri, A., Daie, K., Burdine, R.D., Aksay, E., and Tank, D.W. (2011). Regression-based identification of behavior-encoding neurons during large-scale optical imaging of neural activity at cellular resolution. J. Neurophysiol. *105*, 964–980. https://doi.org/10.1152/jn.00702.2010.

43. Bianco, I.H., Kampff, A.R., and Engert, F. (2011). Prey capture behavior evoked by simple visual stimuli in larval zebrafish. Front. Syst. Neurosci. *5*, 101. https://doi.org/10.3389/fnsys.2011.00101.

44. Easter, S.S. (1972). Pursuit eye movements in goldfish (Carassius auratus). Vision Res. *12*, 673–688. https://doi.org/10.1016/0042-6989(72)90161-7.

45. Fritsches, K.A., and Marshall, N.J. (2002). Independent and conjugate eye movements during optokinesis in teleost fish. J. Exp. Biol. *205*, 1241–1252. https://doi.org/10.1242/jeb.205.9.1241.

46. Vladimirov, N., Mu, Y., Kawashima, T., Bennett, D.V., Yang, C.T., Looger, L.L., Keller, P.J., Freeman, J., and Ahrens, M.B. (2014). Light-sheet functional imaging in fictively behaving zebrafish. Nat. Methods *11*, 883–884. https://doi.org/10.1038/nmeth.3040.

47. Randlett, O., Wee, C.L., Naumann, E.A., Nnaemeka, O., Schoppik, D., Fitzgerald, J.E., Portugues, R., Lacoste, A.M.B., Riegler, C., Engert, F., et al. (2015). Whole-brain activity mapping onto a zebrafish brain atlas. Nat. Methods *12*, 1039–1046. https://doi.org/10.1038/nmeth.3581.

48. Izenman, A.J. (1975). Reduced-rank regression for the multivariate linear model. J. Multivar. Anal. *5*, 248–264. https://doi.org/10.1016/0047-259X(75)90042-1.

49. Semedo, J.D., Zandvakili, A., Machens, C.K., Yu, B.M., and Kohn, A. (2019). Cortical areas interact through a communication subspace. Neuron *102*, 249–259.e4. https://doi.org/10.1016/j.neuron.2019.01.026.

50. Stringer, C., Pachitariu, M., Steinmetz, N., Reddy, C.B., Carandini, M., and Harris, K.D. (2019). Spontaneous behaviors drive multidimensional, brain-wide activity. Science *364*, 255. https://doi.org/10.1126/science.aav7893.

51. Marques, J.C., and Orger, M.B. (2019). Clusterdv: a simple density-based clustering method that is robust, general and automatic. Bioinformatics *35*, 2125–2132. https://doi.org/10.1093/bioinformatics/bty932.

52. Kunst, M., Laurell, E., Mokayes, N., Kramer, A., Kubo, F., Fernandes, A.M., Förster, D., Dal Maschio, M., and Baier, H. (2019). A Cellular-Resolution Atlas of the Larval. Zebrafish Brain. Neuron *103*, 21–38. https://doi.org/10.1016/j.neuron.2019.04.034.

53. Fuchs, A.F., Scudder, C.A., and Kaneko, C.R. (1988). Discharge patterns and recruitment order of identified motoneurons and internuclear neurons in the monkey abducens nucleus. J. Neurophysiol. *60*, 1874–1895. https://doi.org/10.1152/jn.1988.60.6.1874.

54. Sylvestre, P.A., and Cullen, K.E. (1999). Quantitative analysis of abducens neuron discharge dynamics during saccadic and slow eye movements. J. Neurophysiol. *82*, 2612–2632. https://doi.org/10.1152/jn.1999.82.5.2612.

55. Pastor, A.M., De la Cruz, R.R., and Baker, R. (1994). Eye position and eye velocity integrators reside in separate brainstem nuclei. Proc. Natl. Acad. Sci. USA *91*, 807–811. https://doi.org/10.1073/pnas.91.2.807.

56. Daie, K., Goldman, M.S., and Aksay, E.R. (2015). Spatial patterns of persistent neural activity vary with the behavioral context of short-term memory. Neuron *85*, 847–860. https://doi.org/10.1016/j.neuron.2015.01.006.

57. Miri, A., Daie, K., Arrenberg, A.B., Baier, H., Aksay, E., and Tank, D.W. (2011). Spatial gradients and multidimensional dynamics in a neural integrator circuit. Nat. Neurosci. *14*, 1150–1159. https://doi.org/10.1038/nn.2888.

58. Ramirez, A.D., and Aksay, E.R.F. (2021). Ramp-to-threshold dynamics in a hindbrain population controls the timing of spontaneous saccades. Nat. Commun. *12*, 4145. https://doi.org/10.1038/s41467-021-24336-w.

59. Pastor, A.M., Torres, B., Delgado-Garcia, J.M., and Baker, R. (1991). Discharge characteristics of medial rectus and abducens motoneurons in the goldfish. J. Neurophysiol. *66*, 2125–2140. https://doi.org/10.1152/jn.1991.66.6.2125.

60. Aksay, E., Baker, R., Seung, H.S., and Tank, D.W. (2000). Anatomy and discharge properties of pre-motor neurons in the goldfish medulla that have eye-position signals during fixations. J. Neurophysiol. *84*, 1035–1049. https://doi.org/10.1152/jn.2000.84.2.1035.

61. Gonçalves, P.J., Arrenberg, A.B., Hablitzel, B., Baier, H., and Machens, C.K. (2014). Optogenetic perturbations reveal the dynamics of an oculomotor integrator. Front. Neural Circuits *8*, 10. https://doi.org/10.3389/fncir.2014.00010.

62. McFarland, J.L., and Fuchs, A.F. (1992). Discharge patterns in nucleus prepositus hypoglossi and adjacent medial vestibular nucleus during horizontal eye movement in behaving macaques. J. Neurophysiol. *68*, 319–332. https://doi.org/10.1152/jn.1992.68.1.319.

63. Sylvestre, P.A., Choi, J.T.L., and Cullen, K.E. (2003). Discharge dynamics of oculomotor neural integrator neurons during conjugate and disjunctive saccades and fixation. J. Neurophysiol. *90*, 739–754. https://doi.org/10.1152/jn.00123.2003.

64. Beck, J.C., Rothnie, P., Straka, H., Wearne, S.L., and Baker, R. (2006). Precerebellar hindbrain neurons encoding eye velocity during vestibular and optokinetic behavior in the goldfish. J. Neurophysiol. *96*, 1370–1382. https://doi.org/10.1152/jn.00335.2006.

65. Martins, S., Monteiro, J.F., Vito, M., Weintraub, D., Almeida, J., and Certal, A.C. (2016). Toward an integrated zebrafish health management program supporting cancer and neuroscience research. Zebrafish *13* (*Suppl 1*), S47–S55. https://doi.org/10.1089/zeb.2015.1198.

66. Hu, M.-K. (1962). Visual pattern recognition by moment invariants. IEEE Trans. Inf. Theory *8*, 179–187. https://doi.org/10.1109/TIT.1962.1057692.

67. Marquart, G.D., Tabor, K.M., Brown, M., Strykowski, J.L., Varshney, G.K., LaFave, M.C., Mueller, T., Burgess, S.M., Higashijima, S.-I., and Burgess, H.A. (2015). A 3D searchable database of transgenic zebrafish Gal4 and Cre lines for functional neuroanatomy studies. Front. Neural Circuits *9*, 78. https://doi.org/10.3389/fncir.2015.00078.

68. Portugues, R., Haesemeyer, M., Blum, M.L., and Engert, F. (2015). Whole-field visual motion drives swimming in larval zebrafish via a stochastic process. J. Exp. Biol. *218*, 1433–1443. https://doi.org/10.1242/jeb.118299.

69. Hastie, T., Tibshirani, R., and Friedman, J. (2009). The Elements of Statistical Learning: Data Mining, Inference, and Prediction Second (Springer).

![CellPress OPEN ACCESS]

Current Biology
Article

STAR★METHODS

KEY RESOURCES TABLE

REAGENT or RESOURCE	SOURCE	IDENTIFIER
Chemicals, Peptides, and Recombinant Proteins		
UltraPureTM LMP Agarose	Invitrogen	Cat#16520100 https://www.thermofisher.com/order/catalog/product/16520100?SID=srch-hj-16520-100
Sylgard 184	Dow Corning	https://www.dow.com/en-us/pdp.sylgard-184-silicone-elastomer-kit.01064291z.html#overview
Deposited Data		
Z-brain Atlas	https://zebrafishexplorer.zib.de/home/	N/A
Zebrafish Brain Browser (ZBB)	http://vis.arc.vt.edu/projects/zbb/	N/A
mapzebrain Brain Atlas	https://fishatlas.neuro.mpg.de/	N/A
Experimental Models: Organisms/Strains		
Tg(elavl3:Hsa.H2B-GCaMP6s) jf5Tg	Vladimirov et al.[46]	https://zfin.org/action/feature/view/ZDB-ALT-141023-2; RRID:ZFIN_ZDB-ALT-141023-2
Software and Algorithms		
Matlab	Mathworks https://www.mathworks.com/products/matlab.html	https://www.mathworks.com/products/matlab.html MATLAB; RRID:SCR_001622
OpenTK	https://opentk.net/	
Custom matlab code for generating the figures in this study	This study	Mendeley Data, V1: https://doi.org/10.17632/c4wm27z8f6.1
ClusterDv	Marques and Orger[51] https://github.com/jcbmarques/clusterdv	N/A
CMTK	http://neuro.debian.net/pkgs/cmtk.html	Computational Morphometry Toolkit; RRID:SCR_002234

RESOURCE AVAILABILITY

Lead contact
Further information and requests for resources should be directed and will be fulfilled by the lead contact, Claudia E. Feierstein (claudia.feierstein@neuro.fchampalimaud.org).

Materials availability
This study did not generate new reagents.

Data and code availability
All code and pre-processed data to generate the figures in this manuscript are publicly available here: Mendeley: https://doi.org/10.17632/c4wm27z8f6.1. All data reported in this paper will be shared by the lead contact upon request, but it has not been deposited due to its large size.

EXPERIMENTAL MODEL AND STUDY PARTICIPANT DETAILS

Fish care
Adult fish were maintained at 25ºC on a 14:10 hour light cycle following standard methods.[65] Embryos were collected and larvae were raised at 28ºC in E3 embryo medium (5 mM NaCl, 0.17 mM KCl, 0.33 mM CaCl2 and 0.33 mM MgSO4) in groups of 30. Transgenic lines: elavl3:H2B-GCaMP6s, in a nacre (mitfa -/-) background were used (Tg(elavl3:Hsa.H2B-GCaMP6s) jf5Tg[46]; RRID:ZFIN_ZDB-ALT-141023-2). Sexual differentiation occurs at a later larval stage, therefore the sex of the animals cannot be reported. All experimental procedures were approved by the Champalimaud Foundation Ethics Committee and the Portuguese Direcção Geral Veterinária, and were performed according to the European Directive 2010/63/EU.

METHOD DETAILS

Calcium imaging and behavior recording

Five-to-seven-day-old zebrafish larvae were placed in a drop of 1.6% low-melting-temperature agarose (1.6% UltraPureTM LMP Agarose, Invitrogen 16520-100, in E3 water), in a Petri dish with a Sylgard 184 base (Dow Corning) and immersed in E3 water. The agarose around the tail, caudal to the pectoral fins, and eyes was cut away with a fine scalpel to allow for eye and tail movement. The dish was placed onto a light-diffusing screen and imaged on a custom-built two-photon microscope. A Ti-Sapphire laser (Chameleon, Coherent) tuned to 950 nm was used for excitation; power at the sample ranged between 4.2 and 5.6 mW. Frames were acquired at 2 Hz. We imaged the dorsal hindbrain, targeting volumes (width x length x depth) of 369μm x 246μm x 80μm up to 369μm x 246μm x 110μm, which spanned the dorsal aspect of the intermediate and inferior medulla oblongata, situated in rhombomeres 2 to 7. Volumes were imaged as stacks of 80-110 planes in 1μm steps. Each plane was imaged for approximately 125 seconds, the time required for the complete stimulus set (see below). The imaged plane was then shifted by 1 μm. Pixel size was 0.53 μm for x and y.

Visual stimulation

Visual stimuli were displayed using a custom-written rendering engine using OpenTK and the stimuli were generated using OpenGL Shaders (Alexandre Laborde and Lucas Martins, unpublished), and projected at 60 frames per second using an LED projector (Optoma Europe Ltd.). The output of the projector was filtered to allow for simultaneous imaging and visual stimulation (long-pass colored glass filter Thorlabs FGL590 and a TXRED emission filter Thorlabs MF630.9).

The stimulus consisted of radial red and black stripes with a period of 45 degrees. The stimulus was centered on the fish, and was virtually split in two, so that each eye could be stimulated independently. To ensure that the stimulus in one hemifield could not be seen by the other eye, an area in front of the fish spanning an angle of 57.3 degrees was kept unstimulated (black; see schematic in Figure 1A and Video S1). The rotation of the stimulus in each screen-half was modulated independently, with steps of constant velocity (-30, -15, 0, 15, 30 °/s) lasting 5 seconds. A stimulus set or repetition, which consisted of the 25 possible combinations of velocities, was presented in each imaging plane. For each repetition, the order of the velocity pairs varied randomly.

Behavior tracking

To track eye and tail movements, a small hole was cut in the diffusing screen and the fish was imaged from below using a high-speed, infrared-sensitive CMOS camera (Mikrotron EoSens® CL 1362) coupled to a 50 mm objective lens (Schneider Kreuznach Xenoplan 2.8/50-0902) and a pair of filters: a 800 nm short-pass filter (Edmund Optics 64333) and a long pass-filter LP695 (Edmund Optics 32756). Fish were illuminated from above using an infrared LED (M780L2, Thorlabs) through an aspheric condenser diffusing lens (Thorlabs ACL5040-DG6-B) and the microscope objective. Additional illumination for the tail was provided by two infrared LEDs (780 and 800 nm) positioned close to the tail.

Tail data was acquired at 700 Hz, while eye data was acquired at 100Hz. Tail and eye position were extracted online using custom written software (C#). Briefly, eye centers were marked before the beginning of the experiment. The eye object was extracted based on the pixel intensity using the flood fill algorithm. After that, the orientation of the eye object was approximated by calculating the first and second order central image moments. The eye angle was obtained by the angle of the major axis of the approximated eye object relative to the horizontal plane of the image.[66] The angles were then corrected to be defined relative to the midline of the fish; temporal positions were defined as positive (Figure S1A). The starting point of the tail was marked at the caudal part of the swim bladder, and the endpoint was the tip of the tail. The tracking software identified 16 points in between using a sequence of fixed radius sweeps. Tail angles and position, as well as eye angles, were saved to text files for offline analysis.

Anatomical registration

Registration

All registrations were run on Ubuntu server 18.04.4 as a Windows Subsystem Linux instance, using the Computational Morphometry Toolkit (CMTK - http://neuro.debian.net/pkgs/cmtk.html; RRID:SCR_002234) version 3.3.1. The host PC was using a 6 core AMD Ryzen 5 2600 Processor with 64Gb of RAM.

Template

Whole brain anatomical stacks of *elavl3*:H2B-GCaMP6s transgenic zebrafish were obtained by averaging all frames corresponding to a plane. These stacks were acquired with a voxel spacing of 1.13μm x 1.13μm x 1.0μm, and include almost the entire brain (with the exception of the most rostral part of the telencephalon). Seventeen larvae were imaged (6 d.p.f. and 7 d.p.f.), and the seven most complete stacks were selected for template generation.

Templates were generated as follows: one anatomical stack was chosen as a seed, and all other images were registered to this seed using CMTK's registration and warp functions using CMTK's provided wrapper script — munger.pl — (adapted from code at https://github.com/jefferislab/MakeAverageBrain; Greg Jefferis) with options "-X 26 -C 8 -G 120 -R 3". Additional options passed to the Affine and Warp functions were -A "–sampling 2 –accuracy 4 –omit-original-data" and -W "–sampling 2 –accuracy 1.5 –omit-original-data", respectively. When all the registrations were complete, they were used as input to CMTK's avg_adm function to create a shape-averaged greyscale average. This average was then used as the seed for another round of registrations. This process was repeated a total of three times, and the output of the last shape-averaging step was used as the whole-brain *elavl3*:H2B-GCaMP6s template in subsequent steps.

Registrations of functional imaging data to the anatomical template

Hindbrain functional data was registered to the *elavl3*:H2B-GCaMP6s whole-brain template. For each fish, a hindbrain anatomical stack was generated by averaging all frames of a given plane. Hindbrain images had a voxel spacing of 0.53μm x 0.53μm x 1.0μm. After some experimentation, it was determined that these stacks could be registered directly to the anatomical whole brain template by passing a cropping argument ('–crop-index-ref') to CMTK's Registration and Warp functions.

Registrations were performed using munger.pl with options "-X 26 -C 8 -G 120 -R 3". Additional options passed to the Affine and Warp functions were -A "–sampling 2 –accuracy 4 –crop-index-ref 33,89,2,380,391,195" and -W "—sampling 2 –accuracy 1.5 –crop-index-ref 33,89,2,380,391,195", respectively. Finally, to account for excess warping in some of the stacks after registration, munger.pl's "-E" switch was used with some of the registrations to further constrain the weight for grid bending energy. This parameter can vary between 0 and 1, and in these cases was varied from the 0.1 default, up to 0.75. Finally, registrations where the bending energy did not equal 0.1 also used the default 'sampling' and 'accuracy' for the affine and warp steps. Registrations that had good overlap with the template and minimal warping were used in subsequent steps.

The best registrations derived from the above process were then used to drive transformations of the hindbrain anatomical and analysis (correlation, features) stacks associated with that larvae/experiment. Specifically, a shell script (reformat_loop.sh) organized the images and the warp output files to run CMTK function 'reformatx'. Correlation and feature maps were registered to the hindbrain template using CMTK's reformatx function, and nearest neighbor (—nn) interpolation was used in order to preserve the values of the voxels as they were mapped into the reference space

Bridging registrations

The whole-brain *elavl3*:H2B-GCaMP6s template was registered to the ZBB,[67] ZBrain,[47] and MPI2 (https://fishatlas.neuro.mpg.de/) templates using CMTK. To account for differences in the rotations and *z* orientations of the whole-brain *elavl3*:H2B-GCaMP6s template to the external templates, the CMTK registration was seeded with rigid transformations that describe the necessary rotating and flipping of the images. For example, see script munger_bridge_f4wb_mpin.sh; this script seeds the affine transformation with a rigid transformation that rotates the brain to match the rostral/caudal orientation of the MPI template, as well as inverting the z-axis to account for the difference in the order of acquisition of the stack. To account for some undesired warping during bridging to the MPI2 template, the bridging registration was updated to use an energy constraint of 0.5, thus improving the reformatting of individual hindbrains to the MPI2 template.

QUANTIFICATION AND STATISTICAL ANALYSIS

Behavior analysis

All data analysis was performed in MATLAB (MathWorks, USA; RRID:SCR_001622).

Bouts of swimming were extracted from tail angle data as follows. The angle of the tail relative to the body was obtained by calculating the cumulative sum of the angle differences of the first 12 segments (the last 4 segments were excluded as they were too noisy). We then calculated tail vigor as a rolling standard deviation in a window of ∼44 ms (30 frames) of this trace (after Portugues et al.[68]). Bouts were defined as the segments when tail vigor was above a threshold; this threshold was chosen for each fish, based on the distribution of tail vigor values.

To calculate the tail turning bias (which we will simply call *bias*), tail traces were centered by subtracting the median tail deflection angle. Bias was then calculated for each bout. For a bout, bias was defined as the sum of each tail segment deflection angle, divided by the absolute value of that sum (after Haesemeyer et al.[40]). Bouts were classified as forward swims, or left or right turns according to their bias value and a given threshold; thresholds were chosen manually for each fish by analyzing the mean tail traces associated with different threshold values. Absolute bias values greater than the threshold were classified as right/left turns, whereas bias values in between were classified as forward swims. Positive values of bias corresponded to a net rightwards tail bent, while negative values corresponded to a leftwards tail bent.

Eye position was defined as the angle relative to the midline of the fish. Eye position traces were first filtered using a smoothing polynomial filter (Savitzky-Golay filter, order 5, width 15) to denoise the data while preserving the saccades. The data was further smoothed using a median filter in a small window (medfilt1, width 5, corresponding to 50 ms), to further reduce the noise.

Eye velocity was estimated using a differentiator filter to avoid the introduction of high frequency noise when differentiating. Eye position and velocity were then interpolated to match the rate of tail acquisition (700Hz), so that all pieces of behavioral data could be temporally aligned. Eye velocity was decomposed into low, 'following' velocity, and high velocity, which corresponded to saccades. To do so, the velocity trace was first filtered using a median filter (medfilt1, in a window of 9 frames, corresponding to approximately 15 ms), and saccades were defined as points in which velocity was above a threshold, chosen individually for each fish (typically, thresholds were 2 to 4 standard deviations above the mean velocity value). A 'high velocity' or saccade trace was then generated by keeping only the velocities above threshold and setting the rest of the trace to 0. A low velocity trace was generated by removing values above threshold from the velocity trace and replacing them using the 'fillmissing' ('nearest') function in MATLAB. The low velocity trace was further filtered using a running average of 150 points (approximately 250 ms). Throughout the text, we will refer to the desaccaded, low eye velocity, as 'eye velocity', and the high velocity trace as 'saccades'. Temporal eye positions and velocities were defined as positive for both eyes (Figures 1A and S1A).

Eye gain was defined as the ratio of eye velocity divided by the corresponding stimulus velocity. Vergence index was defined as the ratio of the variance of vergent eye positions over the variance of rotating eye positions.

We selected 12 behavioral variables for regression analysis (Figure S2A). The variables included were left/right eye position, left/right (low) eye velocity, left/right high eye velocity (saccades) associated with a bout, left/right high eye velocity (saccades) not associated with a bout, left/right stimulus velocity, tail vigor (which is a measure of swimming) and tail bias (which is a measure of laterality of the tail flick).

Image analysis

Image analysis was performed with MATLAB. Images were corrected for drift or small movements of the fish as previously described.[38] Briefly, each image frame was aligned, using translation only, to the average image of that *z*-plane. Because an interlaced scanning was used, images were aligned first in the horizontal dimension only. Vertical alignments were subsequently performed, but restricted to an integer number of lines. Information about the vertical displacements applied could be used later for reconstructing temporal data. After aligning all frames of a given plane to the average of that plane, consecutive *z*-planes were aligned to each other with subpixel precision. Occasionally, vigorous swimming movements caused a large motion in a single frame. These frames were detected based on (decreased) correlations between consecutive frames and replaced with a linearly-interpolated frame (using the fillmissing function in MATLAB).

Stacks were segmented in overlapping voxels (that we will call ROIs) in the form of cuboids, of 9 x 9 x 9 pixels (4.77 μm x 4.77 μm x 9 μm), tiling the brain in steps of 3 (x,y) or 3 (z) voxels. Note that given the overlap of the ROIs, neurons could be sampled more than once. Because each voxel contained 9 planes, dF/F was computed first for each plane, with F the mean across frames and pixels in a given plane, and dF the difference between the fluorescence value of a given pixel and F. When pulling together *z* planes in a given voxel, dF/F was centered by subtracting the mean across the planes included. This centered dF/F value was used for the subsequent analysis (see Figure 2G for representative ROI traces).

Planes that showed motion artifacts that could not be corrected were excluded from the analysis. If a voxel contained one such plane, the part of the trace corresponding to that plane was excluded.

Data dimensionality

Because our data was acquired sequentially (one plane at a time), it was not possible to determine the dimensionality of the neuronal activity data. To nevertheless get a lower bound on that dimensionality, we performed PCA analysis on subsets of nine sequential planes, in which ROIs were imaged simultaneously, and which were also used to segment the data into cubes/ROIs. As shown in Figures S4E–S4G, in most planes, we find a few components (3-4) that are stronger than the others, although they do not capture a lot of variance (∼30%).

Correlation analysis

Using the initial 12 behavioral variables, we first generated an expanded set of 155 regressors by thresholding eye positions and velocities with various thresholds, by computing eye acceleration, by combining left and right variables, etc. (see Table S1). These variables were downsampled to allow for straightforward alignment to imaging data and used for correlation analysis (Figures 2E and 2F).

To account for delays introduced by the calcium indicator dynamics, we first convolved the expanded set of regressors with a kernel with an exponential decay based on the measured half-decay time for nuclear GCaMP6s (4.68s; our observations), producing a set of predicted fluorescence traces.[38,42] These traces were then compared with the measured fluorescence traces by correlation. Systematic correlation analysis was performed on cuboidal ROIs of 9 x 9 x 9 pixels.

Regression analysis
Criterion for ROI selection

Strictly speaking, a preselection is not necessary for the analysis, as noisy or uncorrelated ROIs do not contribute to the estimation of the features anyway. However, we performed the preselection to maintain computational feasibility. We performed two types of preselection. First, we pre-selected ROIs based on the correlations with a set of 155 regressors (see Table S1 and correlation analysis). ROIs that had a correlation greater than a given threshold with any of the regressors were included in the regression analysis. Second, we generated randomly-selected subsets of ROIs of comparable size. The two selection procedures yielded similar results, although results from the random selection of ROIs were noisier. We also checked that manipulating the selection threshold did not affect the results qualitatively. A threshold of 0.4 was chosen for the analysis in this paper. This resulted in an average of 43,000 (ranging from 27,000 to 57,000) ROIs in each fish.

Regressors

Regressors related to left/right variables were expressed as vergence and rotation, e.g., instead of using 'left eye position' and 'right eye position' as regressors, we used 'eye position vergence', which is simply the sum of the left and right eye positions, and 'eye position rotation', which is the difference between left and right eye positions (Figure S2A). This represents a 45-degree rotation of the coordinate system. This rotated coordinate system is shown as a set of white axes in Figure 1Bi.

For regression analysis, regressors were not convolved with the calcium indicator kernel. Rather, to account for the delay introduced by the indicator, regressors were shifted 20 seconds into the past and 10 seconds into the future, in steps of 0.5 seconds, creating an expanded set of 61 regressors (Figure 3) for each of the 12 regressors. Altogether, we therefore used 732 linearly-independent regressors. Singular value decomposition of the z-scored regressors shows that more than 12 components of the regressor matrix have significant power (Figures S2D and S2E).

Regressors were normalized (z-scored) using the mean and standard deviation of the training set (see estimation of hyperparameters below). For each voxel, fluorescence traces were centered by subtracting the mean fluorescence of its corresponding training set.

Reduced rank regression (RRR)

We sought to relate the measured activity to our set of regressors using multiple linear regression (Figures 3 and S3). To reduce the dimensionality of the population data, we then asked whether activity could be explained by a subspace of our regressor space. To answer this question, we used reduced-rank regression[32,48,49] (RRR).

We started with standard multiple linear regression (MLR), which relates the M×T matrix of regressors (M regressors, T timepoints), X, to the N×T matrix of fluorescence traces (N ROIs, T timepoints), Y,

$$Y = A X \qquad \text{(Equation 1)}$$

where A is a N×M matrix of regression coefficients (Figure S3A). A can be found using the ordinary least squares (OLS) solution so that

$$A_{OLS} = Y X^T \left(X X^T \right)^{-1} \qquad \text{(Equation 2)}$$

To reduce overfitting, we use Ridge Regression,[69] which introduces a regularization term in the matrix inverse so that now

$$A_{Rd} = Y X^T \left(X X^T + \lambda I \right)^{-1} \qquad \text{(Equation 3)}$$

where I is a M×M identity matrix and λ is a constant that establishes the degree of regularization. Large values of λ penalize large regression weights. The predicted ROI traces are then given by

$$\widehat{Y} = A_{Rd} X \text{ (full model)} \qquad \text{(Equation 4)}$$

Because in our experiments planes were recorded sequentially, the matrix Y is incomplete (i.e., we have values for the regressors throughout the experiment, but for each ROI, activity was only measured during part of the experiment). Doing the OLS regression on a matrix of N dependent variables is equivalent to doing N separate OLS regressions, one for each of the dependent variables. Therefore, we do a Ridge Regression for each ROI (using its corresponding regressor trace) and obtain a set of regression coefficients for that ROI. We then construct the matrix A_{Rd} by placing each set of coefficients in a row. This matrix A_{Rd} is now used to calculate $\hat{Y}$. To ensure statistical comparability across ROIs measured in different planes, both the regressors and the activity should ideally be stationary. To ensure stationarity of the regressors, we first analyzed the covariance matrix of the regressors across pairs of planes (Figures S2B and S2C). We then asked whether the regressors for a given plane were 'different' from those of the other planes by looking at the distance of the covariance matrix of that plane to those of the rest (Figure S2B). Planes were considered different from the rest if the mean distance to all other planes was above a threshold (defined f×standard deviations above the mean, where f is a factor to define the threshold; Figure S2C); those planes were removed from the analysis. The stationarity of ROI activities across planes could not be tested, as we did not measure activity of individual ROIs throughout the whole experiment.

To find a subspace of the regressors that could be sufficient to predict Y, we used reduced-rank regression (RRR), which seeks to minimize the mean-square error under a rank constraint on the matrix of regression coefficients, A. Denoting the rank of such a matrix with the index q, we now seek to solve:

$$\widehat{Y}_{RRR} = A_q X \qquad \text{(Equation 5)}$$

such that $\hat{Y}_{RRR}$ is close to Y in the mean-square sense. This can be solved by calculating the singular value decomposition of the predicted traces $\hat{Y}$ obtained using Ridge-regularized OLS (Equation 4),

$$\widehat{Y} = R D W \qquad \text{(Equation 6)}$$

And then setting

$$A_q = R_q R_q^T A_{Rd} \qquad \text{(Equation 7)}$$

where R_q is a matrix composed of the first q columns of the R matrix from the singular value decomposition of $\hat{Y}$. Now we can predict fluorescence activity using Equation 5. The bases of the subspace of 'latent' regressors or *features* that come up in our model is given by a singular value decomposition of the matrix of regression coefficients, A_q:

$$A_q = U S V^T \qquad \text{(Equation 8)}$$

We can therefore rewrite the predicted ROI activity as

$$\widehat{Y}_{RRR} = U S V^T X. \qquad \text{(Equation 9)}$$

Where U has size N×Q and V^T has size Q×M. In turn, we can interpret

$$Z = V^T X \qquad \text{(Equation 10)}$$

as a 'new' and much smaller set of q regressors that can be used instead of the M original regressors, X. This new set of *latent* regressors is built from a linear combination of the original regressors X, with weights given by the columns of the matrix V (Figures 3B and S3B). We will call these columns the *features* associated with the latent regressors. Scaling the features V by multiplying them with the corresponding singular value S results in a scaled version of the feature, that highlights the relative importance of the feature, and we use that form in Figures 4 and S5. The columns of the matrix U indicate how much each of the latent regressors contributes to the activity of each ROI (Figures 3B and S3B). We call these columns the *(feature) contributions*.

One caveat of the RRR analysis is that by focusing on the dominant modes of population activity, one could squeeze out smaller, but still significant modes. For instance, even though the main modes may capture over 90% of the explained variance, there could be smaller pools of neurons that are different and thereby not captured by RRR. While there were no strong outlier ROIs in our comparison of MLR and RRR (Figure 4B), there does appear to be more structure to the clusters in some of the fish (Figure 5). Future work will therefore have to see whether the clusters extracted here need to be refined.

Estimation of hyperparameters

Rank q (the number of features) and the regularization parameter λ were determined using five-fold cross-validation. For each cross-validation fold, 80% of the data were used as a training set, while the remaining 20% of the data were used as a test set. Data was taken in blocks and not randomly sampled to preserve the temporal structure of the traces. The regression weights were always estimated on the training set.

Model performance

Model performance or explained variance (EV) was computed for each ROI as

$$EV = 1 - var\,(y - \hat{y})\,/\,var(y)$$

where y is the fluorescence trace for a given ROI and $\hat{y}$ is the predicted fluorescence trace for that ROI using the full (Ridge-MLR) or the reduced (Ridge-RRR) model. The fluorescence traces and predicted traces were either taken from the training data, yielding the EV on the training set, or from the test data, yielding the EV on the test set.

The average model performance or population explained variance (popEV) was computed for the test set as

$$popEV = 1 - mean\,(var\,(y_i - \hat{y}_i)\,)\,/\,mean\,(\,var\,(\,y_i)\,)$$

where y_i and $\hat{y}_i$ are again the respective traces for a given ROI i, and the mean is taken across all N ROIs. popEV was calculated for a range of values of the regularization parameters q and λ. Finally, we selected the smallest rank q and the largest λ for which the performance of the model was within one standard error of the maximum performance ("one standard error rule"[69]; Figure S4A).

We built separate RRR models for each fish (8 fish). The inputs to the model were a matrix of 732 regressors (X) and a matrix of fluorescence traces (Y) of 45,588 ROIs (median value across fish; see above for selection criteria and RRR formulas).

As a control, and to assess the significance of the contribution (U) values in our models, we built a model where regressors were temporally shuffled to disrupt the relationship with ROI activity. Regressors were shuffled by randomly sorting blocks of 100 points. The resulting model could not explain the data (Figure S4B), and the latent regressor obtained had on average a contribution of zero to population activity (compare U values for the model with real data and that using shuffled regressors, for the same fish; Figure S4C).

Clustering

ROIs were clustered in two ways. First, we clustered ROIs manually. Clustering was performed in feature contribution (U) space, in scatter plots for the contributions of two of the first three latent regressors. We chose the latent regressors that led to the clearest clustering of ROIs; in most cases, this corresponded to the latent regressors associated with features 1 and 2 (six out eight fish; Figure 5A); in two fish this corresponded to the latent regressors associated with features 1 and 3, and 2 and 3. Clusters were defined by manually drawing polygons around the data points (Figures 5B and 5C), following the valleys in the density maps. Only ROIs for which the model's explanatory power was greater than 0.4 were included in the clustering.

Second, ROIs were clustered using ClusterDv,[51] a density-based clustering algorithm that can automatically find the best number of clusters. Clustering was done in 2, 3, 4 and 5 dimensions (when existing), yielding qualitatively identical results. The results using ClusterDv and manual clustering were similar (not shown).

Monocularity index

To estimate the degree of monocular/binocular responses, we computed a monocularity index. For each ROI, this monocularity index was defined as:

$$Monoc\ Index = (max(abs(L)) - max(abs(R))\,/\,(max(abs(L)) + max(abs(R)))$$

Where L and R refer to left and right eye variables. Values around zero correspond to binocular representation of the corresponding eye variable, whereas values of +1 or -1 correspond to monocular representation of left and right eye variables, respectively.